LEVEL II

TECHNICAL REPORT SL-79-15

PROJECTILE PENETRATION IN SOIL AND ROCK: ANALYSIS FOR NON-NORMAL IMPACT

by

Robert S. Bernard, Daniel C. Creighton

Structures Laboratory
U. S. Army Engineer Waterways Experiment Station
P. O. Box 631, Vicksburg, Miss. 39180

December 1979

Final Report

Approved For Public Release; Distribution Unlimited

Prepared for Defense Nuclear Agency
Washington, D. C. 20305

Under DNA Subtask Y99QAXSB211, Work Unit 20

Best Available Copy

Best Available Copy

Unclassified

SECURITY CLASSIFICATION OF THIS PAGE (When Data Entered)

REPORT DOCUMENTATION PAGE		READ INSTRUCTIONS BEFORE COMPLETING FORM
1. REPORT NUMBER (14) WES/TR/ Technical Report SL-79-15	2. GOVT ACCESSION NO.	3. RECIPIENT'S CATALOG NUMBER (9)
4. TITLE (and Subtitle) (6) PROJECTILE PENETRATION IN SOIL AND ROCK: ANALYSIS FOR NON-NORMAL IMPACT.		5. TYPE OF REPORT & PERIOD COVERED Final report, Oct 78 - May 79
		6. PERFORMING ORG. REPORT NUMBER
7. AUTHOR(s) (10) Robert S./Bernard Daniel C./Creighton		8. CONTRACT OR GRANT NUMBER(s)
9. PERFORMING ORGANIZATION NAME AND ADDRESS U. S. Army Engineer Waterways Experiment Station Structures Laboratory P. O. Box 631, Vicksburg, Miss. 39180		10. PROGRAM ELEMENT, PROJECT, TASK AREA & WORK UNIT NUMBERS See Block 18
11. CONTROLLING OFFICE NAME AND ADDRESS Defense Nuclear Agency Washington, D. C. 20305		12. REPORT DATE (11) Dec 1979
		13. NUMBER OF PAGES 88
14. MONITORING AGENCY NAME & ADDRESS(if different from Controlling Office) (12) 92		15. SECURITY CLASS. (of this report) Unclassified
		15a. DECLASSIFICATION/DOWNGRADING SCHEDULE

16. DISTRIBUTION STATEMENT (of this Report)

Approved for public release; distribution unlimited.

17. DISTRIBUTION STATEMENT (of the abstract entered in Block 20, if different from Report)

18. SUPPLEMENTARY NOTES

This research was sponsored by the Defense Nuclear Agency under Subtask (16) Y99QAXSB211, Work Unit 20, "Penetration Support." (17) B211

19. KEY WORDS (Continue on reverse side if necessary and identify by block number)

Ballistics	Penetration
Computer analysis	Projectiles
Impact	Rock penetration
Numerical analysis	Soil penetration

20. ABSTRACT (Continue on reverse side if necessary and identify by block number)

An empirical rigid-projectile analysis has been developed for non-normal impact and penetration into soil and rock. The soil penetration analysis uses Young's S-number as the penetrability index. The rock penetration analysis calculates resistance-to-penetration using density, strength, and Rock Quality Designation. Expressions for compressive normal stress are integrated numerically over the projectile surface using the differential area force law in the

(Continued)

DD FORM 1 JAN 73 1473 EDITION OF 1 NOV 65 IS OBSOLETE

Unclassified

SECURITY CLASSIFICATION OF THIS PAGE (When Data Entered)

411415

20. ABSTRACT (Continued).

PENCO2D computer code. The analysis includes free-surface and wake separation-reattachment effects.

The PENCO2D code is used to make comparison calculations for Sandia/DNA reverse ballistic tests and several full-scale tests conducted by Sandia Laboratories. A parameter study shows effects of soil penetrability, impact velocity, initial attack and obliquity angles, and projectile geometry on underground trajectories.

PREFACE

This investigation was sponsored by the Defense Nuclear Agency under Subtask Y99QAXSB211, "Penetration," Work Unit 20, "Penetration Support." This study was conducted by personnel of the Structures Laboratory (SL), U. S. Army Engineer Waterways Experiment Station (WES), during October 1978 through May 1979, under the general supervision of Mr. Bryant Mather, acting Chief, SL, and Dr. J. G. Jackson, Jr., Chief, Geomechanics Division (GD), SL. Mr. R. S. Bernard formulated the theory, and Mr. D. C. Creighton developed and implemented the computer analysis, both under the technical guidance and direction of Dr. B. Rohani, GD. Messrs. Bernard and Creighton prepared this report.

COL John L. Cannon, CE, and COL Nelson P. Conover, CE, were Commanders and Directors of WES during the period of research and report preparation. Mr. F. R. Brown was Technical Director.

CONTENTS

LIST OF TABLES

LIST OF FIGURES

Figure		Page

CONVERSION FACTORS, U. S. CUSTOMARY TO METRIC (SI) UNITS OF MEASUREMENT

U. S. customary units of measurement used in this report can be converted to metric (SI) units as follows:

Multiply	By	To Obtain
feet	0.3048	metres
inches	0.0254	metres
feet per second	0.3048	metres per second
pounds (force) per foot	14.5939	newtons per metre
pounds (force) per square inch	6894.757	pascals
pounds (mass)	0.4535924	kilograms
pounds (mass) per cubic foot	16.01846	kilograms per cubic metre
pounds (mass) per inch	17.85797	kilograms per metre
pounds (mass)-square inches	0.0002926	kilograms-square metres

PROJECTILE PENETRATION IN SOIL AND ROCK: ANALYSIS FOR NON-NORMAL IMPACT

CHAPTER 1

INTRODUCTION

1.1 BACKGROUND

In recent years, due to growth of the experimental data base, development of empirical formulas, and implementation of new theoretical and computational techniques, it has become possible to predict the approximate motion of stable earth penetrators after normal impact in many types of geological targets (Reference 1-4). Results of some non-normal (yawed/oblique) impact tests have also been predicted successfully, although the data base is small compared to that for normal impact (References 5 through 7).

Previous analyses by the U. S. Army Engineer Waterways Experiment Station (WES) of non-normal impact have used the Cavity Expansion Theory (CET) for rock, and an empirical formulation similar to Young's equation for soil (References 5 and 8). These analyses were considered preliminary when they were first developed, and it was hoped that more credible analyses would arise in the future.

1.2 PURPOSE AND SCOPE

The present investigation concerns the development of a generalized analysis for oblique/yawed impact and penetration in soil and rock (or rock-like) targets, based on the modification of previous analyses and the interpretation of recent test data. The objectives are (a) to obtain external load-time histories sufficiently accurate for structural response calculations and (b) to calculate postimpact trajectories well enough to predict the terradynamic performance and stability of a given projectile.

The two-dimensional (2-D) penetration theory, including equation of motion, stress distribution, and free-surface and wake separation-reattachment effects, was developed. The penetration theory was computer coded into PENCO2D to make comparison calculations with experimental data from both reverse ballistic and conventional penetration tests. Using PENCO2D, the effects of initial impact conditions, projectile geometry, and soil penetrability were examined in a brief parameter study.

CHAPTER 2

PENETRATION ANALYSIS FOR MOTION IN TWO DIMENSIONS

2.1 PROJECTILE MOTION IN TWO DIMENSIONS

Consider a rigid, deeply buried projectile (no free-surface effects), whose motion lies in the XZ-plane,[1] as shown in Figure 2.1. The rotation is described by the angular velocity $\dot{\theta}$, and the translation by $\dot{X}$ and $\dot{Z}$, the X- and Z-velocity components of the center of gravity (CG).[2,3] For analysis, it is convenient to express the CG velocity in terms of its lateral and axial (x- and z-) components V_x and V_z , respectively:[4]

$$V_x = \dot{X} \cos \theta - \dot{Z} \sin \theta \tag{2.1}$$

$$V_z = \dot{X} \sin \theta + \dot{Z} \cos \theta \tag{2.2}$$

For purely axial motion ($V_x = 0$, $\dot{\theta} = 0$), the stress distribution on the projectile is symmetric, and the net force is in the axial direction, producing no pitch (turning) moment. The introduction of rotation ($\dot{\theta} \neq 0$) or lateral motion ($V_x \neq 0$) destroys this symmetry, and it is necessary to specify the asymmetric stress distribution in order to calculate the resulting force and moment.

Suppose that the compressive resisting stress σ is always normal to the projectile surface (no tangential stresses). On any surface area element dA , the x- and z-components of σ are, respectively,

---

1 The XZ-coordinate system is fixed in the target (Figure 2.1).

2 A dot above any quantity indicates differentiation with respect to time.

3 For convenience, symbols and abbreviations used in this report are listed and defined in the Notation, Appendix C.

4 The xz-coordinate system is fixed on the projectile axis, with its origin at the CG (Figure 2.1). Equations 2.1 and 2.2 represent the projections of the absolute velocity vector along the x- and z-axes.

$$\sigma_x = \sigma \cos \eta \cos \psi \tag{2.3}$$

$$\sigma_z = \sigma \sin \eta \tag{2.4}$$

where

ψ = azimuthal angle (Figure 2.2)

$\tan \eta$ = slope of projectile surface at a given point, with respect to axis of symmetry (Figures 2.1 and 2.3)

The lateral and axial force components (Figure 2.2) acting on surface element dA are, respectively,

$$dF_x = -\sigma_x \, dA \tag{2.5}$$

$$dF_z = -\sigma_z \, dA \tag{2.6}$$

where dA is the differential element of surface area. The lateral and axial net force components acting on the entire projectile are then

$$F_x = -\int \sigma_x \, dA \tag{2.7}$$

$$F_z = -\int \sigma_z \, dA \tag{2.8}$$

where the integral is evaluated over the entire projectile surface. The translational (CG) equations of motion are

$$M \ddot{X} = F_x \cos \theta + F_z \sin \theta \tag{2.9}$$

$$M \ddot{Z} = -F_x \sin \theta + F_z \cos \theta \tag{2.10}$$

where M is the projectile mass and $\ddot{X}$ and $\ddot{Z}$ are the components of acceleration in the X- and Z-directions, respectively. The projectile is assumed to be rigid, so the rotational equation of motion is

$$I\ddot{\theta} = \int z \, dF_x - \int x \, dF_z \tag{2.11}$$

where I is the transverse mass moment of inertia about the CG, $\ddot{\theta}$ is the angular acceleration, and x and z are the lateral and axial distances, respectively, from the CG (Figure 2.1). The right-hand side of Equation 2.11 is the total moment exerted on the projectile about its CG, and the integrals are evaluated over the entire area of the projectile surface.

2.2 STRESS DISTRIBUTION FOR ROCK AND CONCRETE

For penetration into concrete and intact rock (Appendix A), the net force on the projectile can be calculated approximately from the following normal stress distribution:

$$\sigma = \begin{cases} 1.582\left(4Y + 3v\sqrt{\rho Y}\right)\sqrt{\dfrac{v_n}{v}}, & v_n \geq 0 \\ 0, & v_n \leq 0 \end{cases} \tag{2.12}$$

where

- Y = unconfined compressive strength of intact target material[5]
- ρ = target mass density
- v = absolute local velocity of a given point on projectile surface (Figure 2.3)
- v_n = outward normal component of v (Figure 2.3)

Defined in terms of V_x, V_z, $\dot{\theta}$, and z, the quantities v and v_n are

$$v = \left[V_z^2 + \left(V_x + z\dot{\theta}\right)^2\right]^{1/2} \tag{2.13}$$

---

[5] If necessary, minor corrections to Y can be made for the quality of the rock or for the maximum aggregate size in the concrete (Appendix A). Any set of units can be used in Equation 2.12 but they must be dimensionally compatible (e.g., slugs, feet, seconds).

$$v_n = V_z \sin \eta + (V_x + z\dot{\theta}) \cos \eta \cos \psi \qquad (2.14)$$

It is assumed that a given surface element must have a net motion <u>into</u> the target material to produce a resisting stress; hence, σ vanishes when $v_n \leq 0$ in Equation 2.12.

2.3 STRESS DISTRIBUTION FOR SOIL

For penetration into soil (Appendix B), the net force on the projectile can be calculated approximately from the following normal stress distribution:[6]

$$\sigma = \begin{cases} \dfrac{0.625\,\mu}{S\,r_p}\sqrt{\dfrac{v_n}{v}} + \dfrac{5.19\,v}{S}\sqrt{\beta\,r_p\,\dfrac{v_n}{v}} + \dfrac{5.9\,\gamma Z}{S^2}\,\dfrac{v_n}{v}\,, & v_n \geq 0 \\[2ex] 0\,, \quad v_n \leq 0 \end{cases} \qquad (2.15)$$

where

$\mu = 1.96 \times 10^5$ lb/ft, constant[7]

$\beta = 6.25 \times 10^6$ lb^2-sec^2/ft^7, constant

$\gamma = 1.56 \times 10^5$ lb/ft^3, constant

S = Young's S-number (Appendix B), soil penetrability index

r_p = local cylindrical radius at a given point on the projectile surface

Z = vertical depth of a given point on the projectile surface, measured from the target surface

The expressions for v and v_n are still given by Equations 2.13 and 2.14, respectively; and the requirement that $v_n > 0$ for $\sigma > 0$ applies in soil as well as in rock or concrete.

The quantities μ, β, and γ are constants, independent of soil

---

6 Any set of dimensionally compatible units can be used in Equation 2.15, as long as <u>all</u> quantities are converted to those units.

7 A table of factors for converting U. S. customary units of measurement to metric (SI) units is presented on page 6.

type and projectile characteristics. Thus, the only parameter characterizing the soil is Young's empirical S-number, which can be obtained for a given target from previous penetration data or from correlation with geological descriptions (Table B.1).

2.4 WAKE SEPARATION AND REATTACHMENT

Flash X-ray photographs and two-dimensional (2-D) finite-difference calculations have shown that loss of contact between target and projectile occurs somewhere on the nose, while reattachment may or may not occur on the aftbody. The current analysis is not sophisticated enough to predict the actual onset of separation. Nevertheless, it is necessary to include a simple model for the kinematics of wake separation, especially when 2-D projectile motion in soil is investigated.

It is assumed that there is a minimum angle of approach, or wake separation angle, ϕ_{min} required between the target and the projectile contact surface (Figure 2.4) in order for contact to be maintained. For a given surface element, the local angle of approach ϕ is determined by the instantaneous orientation[8] of the projectile such that

$$\sin \phi = \frac{V_n}{V} \tag{2.16}$$

where V is the CG velocity and V_n is its outward component normal to the projectile surface, given by

$$V_n = V_z \sin \eta + V_x \cos \eta \cos \psi \tag{2.17}$$

Thus, separation occurs whenever $\phi \leq \phi_{min}$, i.e., whenever the local angle of approach is less than the wake separation angle.[9]

Separation is only part of the problem; reattachment may or may

---

[8] The rotational velocity $\dot{\theta}$ is not considered in formulating the criterion for wake separation. This quantity does, however, play a strong role in wake reattachment.

[9] For the case of no yaw (no angle of attack), Equation 2.16 reduces to $\sin \phi = \sin \eta$.

not occur, depending on the relative motion of the wake and the aftbody downstream of the separation point. It is expected that the wake separation angle ϕ_{min} will generally be small (<10 degrees), in which case the angle of attack α required to maintain contact will also be small. In any case, reattachment will be analyzed based on three assumptions:

1. Constant axial velocity (V_z)
2. Constant angular velocity ($\dot{\theta}$)
3. Constant angle of attack (α)

Obviously, these three quantities change as the projectile penetrates into the target. Nevertheless, if the quantities do not vary rapidly, the quasistatic approximation is adequate.

The cavity formed by the wake is a gently curved cylindrical tube of increasing radius (with time), and the projectile rotates inside this tube as it travels forward. The curved axis of the cavity is fixed in the target, and aftbody reattachment occurs wherever the projectile rotates into the cavity wall (Figure 2.5).

Disregarding any stresses that may oppose the radial expansion of the cavity, conservation of mass and incompressibility in the target requires that

$$r_c \dot{r}_c = \text{constant} \tag{2.18}$$

where r_c is the local cylindrical wake-cavity radius. Evaluating Equation 2.18 at the separation point, it then follows that

$$r_c \dot{r}_c = r_o V_z \tan \phi_{min} \tag{2.19}$$

where r_o is the projectile radius at the separation point. For small values of ϕ_{min}, r_o is approximately the radius corresponding to $\eta = \phi_{min}$ (Figure 2.4). Furthermore, for straight- and tapered-aftbody projectiles, r_o is approximately the radius at the base of the nose.

Denoting axial distance aft of the nose tip by ζ, time derivatives can be related to V_z and ζ by the transformation

$$\frac{d}{dt} = V_z \frac{d}{d\zeta} \tag{2.20}$$

and Equation 2.19 reduces to

$$r_c \frac{dr_c}{d\zeta} = r_o \tan \phi_{min} \tag{2.21}$$

for which the solution is

$$r_c = \sqrt{r_o^{\,2} + 2r_o \left(\zeta - \zeta_o\right) \tan \phi_{min}} \;, \quad \zeta \geq \zeta_o \tag{2.22}$$

where ζ_o is the value of ζ at the separation point. For $\zeta < \zeta_o$, the cavity radius is the same as the projectile radius, since no loss of contact has occurred.

Using Equation 2.20 again, the differential equation for the lateral displacement δ of a point on the projectile axis, relative to the cavity centerline (Figure 2.5), is

$$\frac{d\delta}{dt} = V_z \frac{d\delta}{d\zeta} = \zeta - \zeta_o \quad \dot{\theta} \tag{2.23}$$

Treating V_z and $\dot{\theta}$ as constants, the solution for δ is

$$\delta = \frac{1}{2} \left(\zeta - \zeta_o\right)^2 \frac{\dot{\theta}}{V_z} + \delta_o \tag{2.24}$$

The initial displacement $\delta_o = \zeta \sin \alpha$ is the displacement due to the angle of attack α (treated here as a constant),[10] so Equation 2.24 is replaced by

---

[10] It is assumed that small attack angles do not significantly change the cavity geometry. Thus, if $\dot{\theta} = 0$, the cavity centerline will be straight; but if in addition $\alpha \neq 0$, the projectile axis will be skewed relative to the cavity, producing displacements $\delta_o = \zeta \sin \alpha$ between the projectile axis and the cavity centerline.

$$\delta = \frac{1}{2} (\zeta - \zeta_o)^2 \frac{\dot{\theta}}{V_z} + \zeta \sin \alpha \tag{2.25}$$

where

$$\alpha = -\tan^{-1}\left(\frac{V_x}{V_z}\right) \tag{2.26}$$

At any point on the projectile surface aft of the separation point, the criterion for <u>no contact</u> is[11]

$$\left.\begin{aligned} &\frac{1}{2} (\zeta - \zeta_o)^2 \frac{\dot{\theta}}{V_z} + \zeta \sin \alpha - r_p \cos \psi < \sqrt{r_c^{\,2} - r_p^{\,2} \sin^2 \psi}\ , \quad \frac{\pi}{2} \le \psi \le \frac{3\pi}{2} \\ &r_p \cos \psi - \frac{1}{2} (\zeta - \zeta_o)^2 \frac{\dot{\theta}}{V_z} - \zeta \sin \alpha < \sqrt{r_c^{\,2} - r_p^{\,2} \sin^2 \psi}\ , \quad -\frac{\pi}{2} \le \psi \le \frac{\pi}{2} \end{aligned}\right\} \tag{2.27}$$

Hence, if $\phi \le \phi_{min}$ <u>and</u> Equation 2.27 are satisfied, there is no contact, and $\sigma = 0$.

The foregoing analysis is only a rough method of accounting for wake separation and reattachment using a single input parameter, the wake separation angle ϕ_{min} . Nevertheless, this analysis does make it possible to assess the relative effects of separation and reattachment on projectile stability, as will be shown in Chapter 3.

2.5 FREE-SURFACE EFFECT

In brittle materials, such as rock and concrete, a crater is always formed during (or just after) impact. Postimpact inspections in rock (Reference 9) indicate that these craters may be as much as 10 projectile diameters across at the target surface. The crater width decreases

---

[11] Figure 2.6 presents a rear axial view of the projectile and cavity cross sections at an arbitrary location aft of the separation point. The figure is valid only for small displacements, i.e. $\delta \ll \zeta$.

rapidly with depth, however, approaching a value equal to (or slightly less than) the projectile diameter after a few calibers of penetration. The same phenomenon occurs in soil, though to a lesser extent than in rock, since soils are more ductile than brittle in behavior.

For normal impact or for near-normal impact with slight yaw, it is not necessary to account for the cratering phenomenon (i.e., free-surface effect) in calculating the loads on the projectile with the current analysis. On the other hand, for oblique impact with no initial yaw, the free-surface effect is probably one of the dominant mechanisms creating an unbalanced lateral force on the projectile, especially in rock and concrete. Thus, for analyzing non-normal impact in general, the presence of the free surface should be acknowledged, even if only by a crude representation of its effect.

The influence of the free surface is modeled herein with an on-off stress criterion, governed by the location of a given projectile surface element dA with respect to the free surface (Figure 2.7). Whenever the radial distance from the projectile axis (through dA) to the free surface is less than some prescribed value r_s,[12] then the stress on dA is set equal to zero. Quantitatively, this condition is expressed by setting $\sigma = 0$ whenever

$$Z_{CG} + z \cos \theta < r_s \sin \theta \cos \psi \qquad (2.28)$$

where Z_{CG} is the vertical distance from the free surface to the CG. Assuming r_s to be directly proportional to the local projectile radius r_p, Equation 2.28 is replaced by the stipulation that $\sigma = 0$ whenever

$$Z_{CG} + z \cos \theta < kr_p \sin \theta \cos \psi \qquad (2.29)$$

where the free-surface parameter is

---

12 r_s is the maximum perpendicular distance from projectile axis, through dA, to target surface for which stress relief due to the free surface can occur.

$$k = \frac{r_s}{r_p} = \text{constant} \tag{2.30}$$

This model for the free-surface effect produces a stress distribution that may be partially or completely turned off on the top side ($-\pi/2 < \psi < \pi/2$) of the projectile, depending on the geometry, depth, and orientation with respect to the target surface. The deeper the penetration and the more vertical the orientation, the smaller the influence of the free surface on the lateral loads.

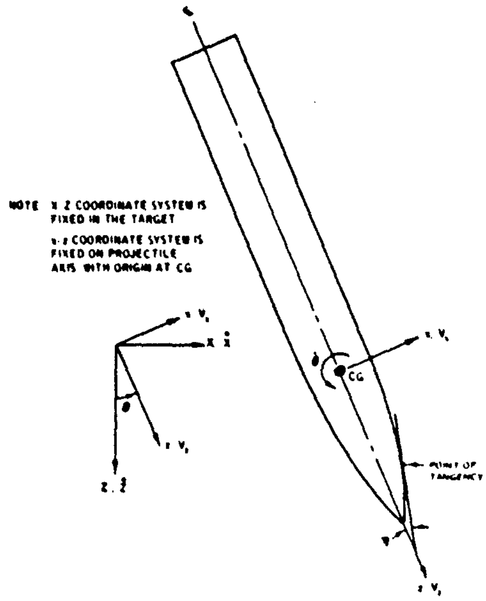

Figure 2.1 Projectile motion in two dimensions.

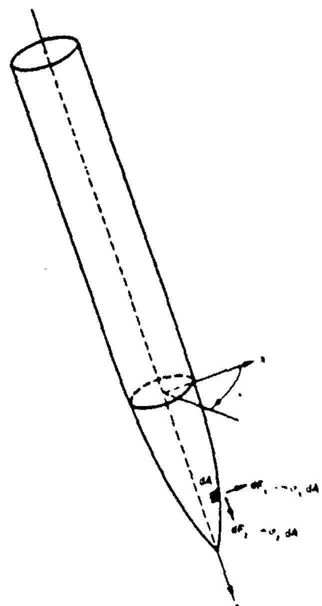

Figure 2.2 Three-dimensional view of projectile.

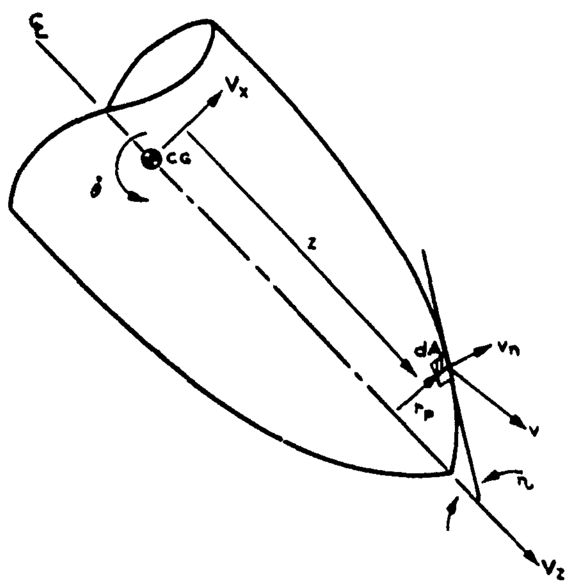

Figure 2.3 Projectile surface geometry and velocity components.

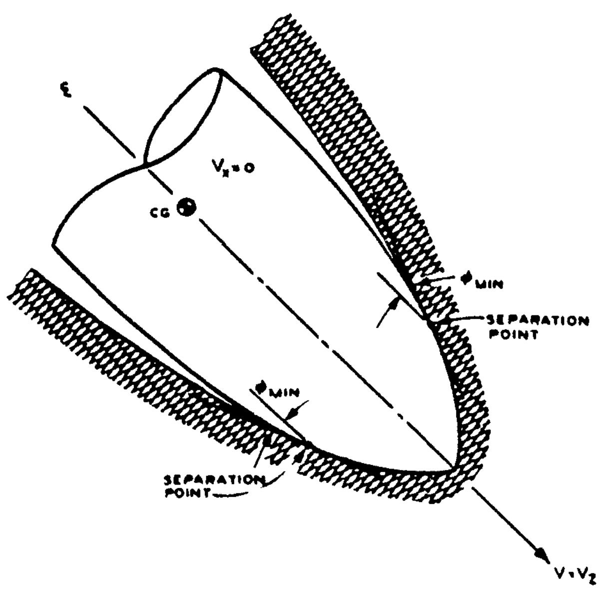

Figure 2.4 Wake separation for purely axial motion.

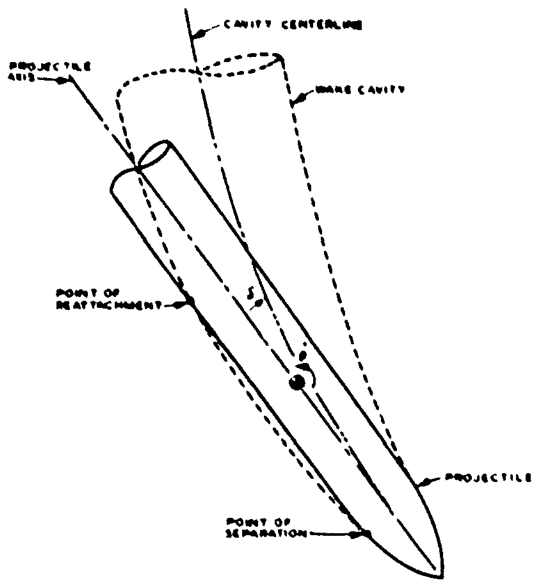

Figure 2.5 Separation and reattachment on a rotating projectile.

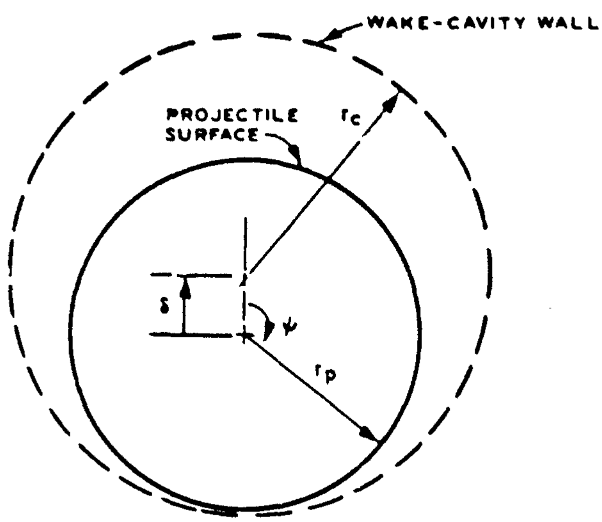

NOTE. THIS DRAWING VALID ONLY FOR $\delta \ll \zeta$

DISPLACEMENT RELATIVE TO WAKE-CAVITY CROSS SECTION AFT OF SEPARATION POINT

Figure 2.6 Rear axial view of projectile cross section.

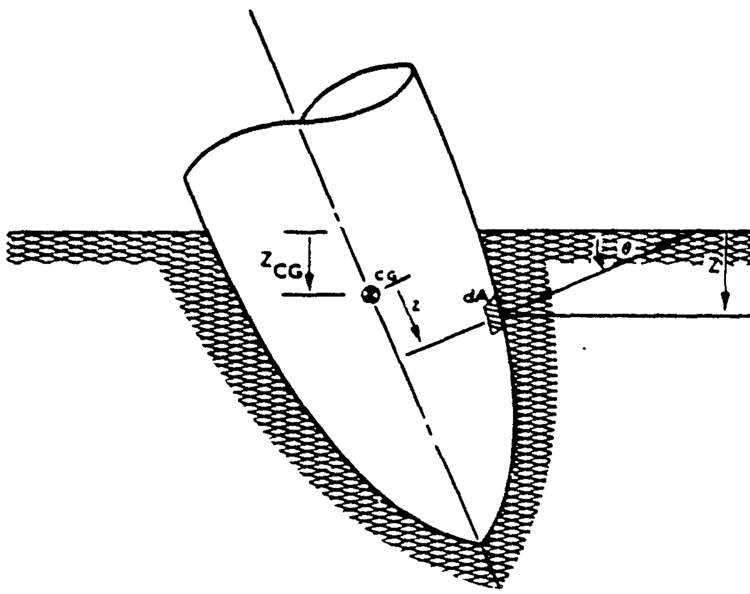

Figure 2.7 Projectile orientation with respect to free surface.

CHAPTER 3

CALCULATIONS AND EXPERIMENTAL DATA

3.1 BACKGROUND

Detailed information concerning non-normal impact effects is scarce, mainly because additional parameters that go beyond those important for normal impact are involved. In the latter case, the important quantities are the weight, size, and geometry of the projectile; the impact velocity; the final depth; and the axial deceleration record. For non-normal tests, however, the additional important parameters are the moment of inertia and CG of the projectile, the lateral components of the impact velocity, the 2- or 3-D trajectory (including projectile orientation), and the lateral components in the deceleration record.

Usually, the only way to obtain all this information is by conducting a reverse ballistic test (RBT). Still, if the projectile parameters are known, much insight can be gained from knowing only the impact conditions and the final position, particularly with regard to stability.

In this chapter, comparisons will be made between calculations[1] and test results for RBT's and conventional penetration tests. The main purpose will be to investigate the general credibility of the analysis and the parameters used therein. Although the data are too few to achieve the degree of verification that can be obtained for normal impact, there are still enough benchmarks available to check for unreasonable predictions. With this done, some credence can be given to the parameter study in Chapter 4.

3.2 REVERSE BALLISTIC TESTS IN SANDSTONE

In 1977, Sandia Laboratories conducted four DNA-sponsored RBT's in sandstone. A complete description of the tests is given in Reference 10,

[1] The PENCO2D computer code, which solves the penetration problem in two dimensions, using the analysis presented in Chapter 2, was used for all calculations reported herein.

and the processed data are presented in References 11 and 12. Two of the tests (Nos. 2 and 3) were done at a 3-degree attack angle, and one (No. 4) at 20 degrees obliquity (no angle of attack). The impact velocity was approximately 1500 ft/s in each case. Nominal target properties are[2]

$$\rho = 130 \text{ lb/ft}^3$$

$$Y = 3400 \text{ psi}$$

$$\text{Rock quality designation (RQD)} = 100$$

A scale drawing of the projectile is shown in Figure 3.1; the projectile parameters are[2]

$$\text{Length (L)} = 18.15 \text{ in}$$

$$\text{Weight (W)} = 9.48 \text{ lb}$$

$$\text{Diameter (D)} = 1.9 \text{ in}$$

$$\text{Caliber radius head (CRH)} = 6.00 \text{ (beveled tip)}$$

$$I = 221.9 \text{ lb-in}^2$$

For each case, the load distributions on the projectile, calculated using the PENCO2D computer code (with output modifications), have been used as input to a dynamic structural-response code (WHAMS) by T. Belytschko.[3] Predictions were generated for accelerometer and strain-gage outputs, samples of which are compared with test results in Figures 3.2 through 3.7. In the WHAMS calculations, the accelerometers indicated in Figures 3.2 and 3.3 were located on the axis, 16.35 inches from the nose tip. The strain gage was on the outside

---

2 The units shown were chosen for convenience of expression. In calculations they must be converted to a compatible system (e.g., slugs, feet, seconds).

3 Personal communication, received March 1979, from T. Belytschko, Inc., Chicago, Ill., to R. Bernard, Geomechanics Division, Structures Laboratory.

bottom ($\psi = \pi$), 9.6 inches from the nose tip.

For the 3-degree attack angle calculation, there is clearly a phase difference between the calculated and measured lateral accelerations (Figure 3.2), the cause of which is not yet understood. Also, the initial positive peaks in the calculated results are somewhat low, but the later negative peaks are in fair agreement with the test data. Better agreement exists for the axial decelerations (Figure 3.3). Fair agreement is obtained for the strain gage output (Figure 3.4), although the initial negative strains are somewhat underpredicted.

For the 20-degree obliquity calculation, the calculated results are in much better agreement with the test data (Figures 3.5 through 3.7), although the phase-difference problem is still apparent in the lateral acceleration (Figure 3.5) data and the strain gage output (Figure 3.7).

In using the PENCO2D computer code to generate the input for Belytschko's WHAMS calculations, the free-surface parameter was set at $k = 8$, and the wake separation angle was set at $\phi_{min} = 0$. These values were chosen after examining the effect of varying k and ϕ_{min} in WES predictions for total lateral force and pitch moment (Figures 3.8 through 3.13).[4] The value $k = 8$ is reasonable in light of penetration-crater measurements in sandstone (Reference 9), and the $\phi_{min} = 0$ value is reasonable, since the wake separation angle should be small in hard targets.

In order to examine the effects of attack angle and obliquity on lateral load and pitch moment in the WES theory, a series of calculations has been made using the 3- and 20-degree RBT's as baseline cases. The results are shown in detail in Figures 3.14 through 3.17 and summarized in Figures 3.18 and 3.19. A similar series of calculations was made, varying the target strength for the 3-degree RBT. The results, shown in Figures 3.20 and 3.21, indicate that the initial peaks in the lateral force (at 0.12 ms) are much more dependent on strength than are the later peaks (at 0.7 to 0.8 ms). The reason for the similarity in the

[4] Variation of k has no discernible effect on the 3-degree RBT calculation.

later peaks can be seen by examination of the lateral force distribution (per unit length) at 0.7 ms (Figure 3.22). The amplitude of the force distribution is a strong function of the strength, but the positive and negative contributions are such that there is little difference in the net lateral force at 0.7 ms.

3.3 FULL-SCALE PENETRATION TESTS IN SOIL

Sandia Laboratories has conducted at least four full-scale soil penetration tests that are suitable as benchmarks for the WES 2-D penetration theory. Two of these tests, Nos. R800915 and R800916 (Reference 13), were conducted in the Pedro dry lake site on Tonopah Test Range (TTR). The other tests, Nos. R454025-22 and R454025-23 (Reference 14), took place in the Antelope dry lake site on TTR. Pertinent information for all four tests is summarized in Table 3.1, and Young's S-number profile (Reference 14) for the Antelope site is given in Table 3.2.

Using the information given in Tables 3.1 and 3.2 as input, calculations have been made for the penetrator trajectories. The results are compared with the Sandia test data in Figures 3.23 through 3.27.

Calculations for tests R800915 and R800916, presented respectively in Figures 3.23 and 3.24, show the effects of varying the wake separation angle. Here the experimental results are inconsistent. The tests were identical except for a 20 percent difference in impact velocity, yet there was a 500 percent difference in lateral (horizontal) displacement.[5] One of the reasons for the discrepancy may have been a difference in the amount of wake separation in the two tests. Separation alone, however, is not enough to account for the difference, since even the calculation for $\phi_{min} = 0$ predicts 8 feet of lateral displacement for test R800915. In these calculations the free-surface parameter was

[5] The average vertical penetration resistance apparently was the same, because the depths can be calculated with same S-number.

set at $k = 0$, due to its lack of influence on near-vertical impact problems.

Test R454025-23 is a good example for assessing the effects of the free-surface parameter independent of the wake separation angle effects. Here the initial obliquity is large, and k and ϕ_{min} both influence the calculated trajectory (Figures 3.25 and 3.26). For this test the best simulation of the observed trajectory is obtained for $k = 4$ and $\phi_{min} = 0$.[6] Nevertheless, it is clear from the calculations that the wake separation angle has a much stronger influence than the free-surface parameter, even for large obliquity.

Test R454025-22 was conducted with a shorter projectile (L/D = 8) than the other three tests (L/D = 10). In this case, the penetrator impacted at 30 degrees and rotated 80 degrees before coming to rest 13.5 feet below the target surface. With the free-surface parameter set at $k = 4$, calculations made for different values of the wake separation angle (Figure 3.27) indicate that a value of $\phi_{min} = 4$ degrees best reproduces the observed final position of the penetrator.

In other (normal impact) tests[7] in the Antelope site, Sandia has found L/D = 10 to be significantly more stable than L/D = 8 (Reference 14). For comparison of the two projectiles in this study, calculations were made for the shorter projectile (from test R454025-22) using the S-number and impact conditions of test R800916, setting $k = 0$, and varying ϕ_{min} . The results (Figures 3.28-3.31) indicate that the stability of either projectile is strongly dependent on the value selected for the wake separation angle.

---

[6] To simulate the test conditions (Table 3.1), the calculation was started with the nose tip at $Z = 8$ inches .

[7] $\theta = 2$ degrees, $\alpha < 0.5$ degrees.

Table 3.1. Soil penetration data for non-normal impact.

Sandia Test No.	Projectile Description: Total Weight lb	Maximum Diameter in	Total Length in	CRH	Distance to CG in	Moment of Inertia $lb\text{-}in^2$	Target Description	Impact Conditions: Impact Velocity ft/s	Obliquity Angle[a] deg	Attack Angle deg	Trajectory: Final Depth ft	Final Range ft	Path Length ft	Remarks
R800915	350	6.125	61.25	6.0	32.2	9.63×10^4	TTR Pedro dry lake site; S ≈ 3.8[b]	1400	3.7	3.7	49	2.5	49.1	Stable motion; projectile deviated in direction of attack angle
R800916	350	6.125	61.25	6.0	32.2	9.63×10^4	TTR Pedro dry lake site; S ≈ 3.8[b]	1680	3.7	3.7	58	13	59.4	Stable motion; projectile deviated in direction of attack angle
R454025-22	320	6	48	9.25	27.7	4.26×10^4	TTR Antelope dry lake site; see Table 3.2	2333	30	<0.5	13.5		130	Rotated 80 deg and stopped 13.5 ft below surface at angle of 20 deg from horizontal
R454025-23	400	6.5	65	9.25	32.45	1.06×10^5	TTR Antelope dry lake site; see Table 3.2	1617	75	<0.5			125.5	Stable motion;[c] rotated 2 deg toward surface

[a] Obliquity angle in plane of motion.
[b] Average S-number, back-calculated using Equation B.4 in Appendix B.
[c] Impact point was 6 in below ground surface. Shallow cut had been made in soil so that projectile axis was normal to impact surface.

Table 3.2. S-number profile for TTR Antelope Dry Lake site.[a]

Depth, ft		
From	To	S-number
0	27	5
27	35	2.5
35	50	5.5
50	80	7
80	85	3
85	109	8
109	170	11.5
170	∞	13.5

[a] From Reference 14.

STATION	AXIAL DISTANCE FROM NOSE TIP INCHES	SIGNIFICANCE
B	3.80	NOSE BASE
CG	8.71	CENTER OF GRAVITY
F	8.20	FORWARD ACCELEROMETER
R	17.30	REAR ACCELEROMETER
S	9.60	STRAIN GAGE

NOTE: FLARE BEGINS AT 9.64 IN AND
ENDS AT 13.04 IN
TOTAL LENGTH L = 18.15 IN

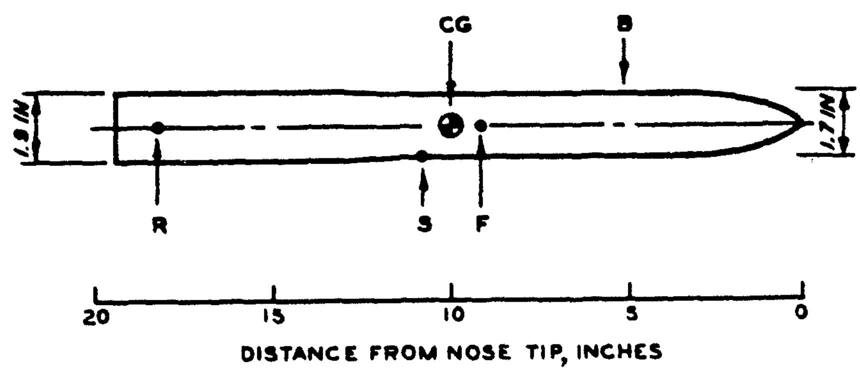

Figure 3.1 Scale drawing of RBT penetrator.

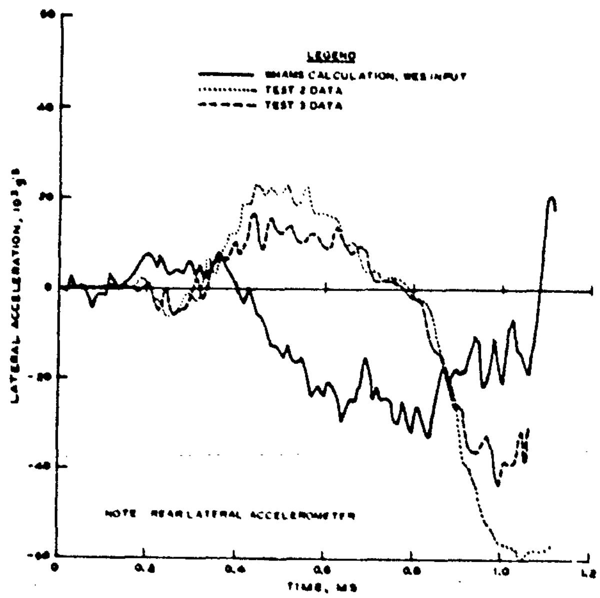

Figure 3.2 Comparison of calculated and measured lateral accelerations for Sandia/DNA RBT, 3-degree attack angle.

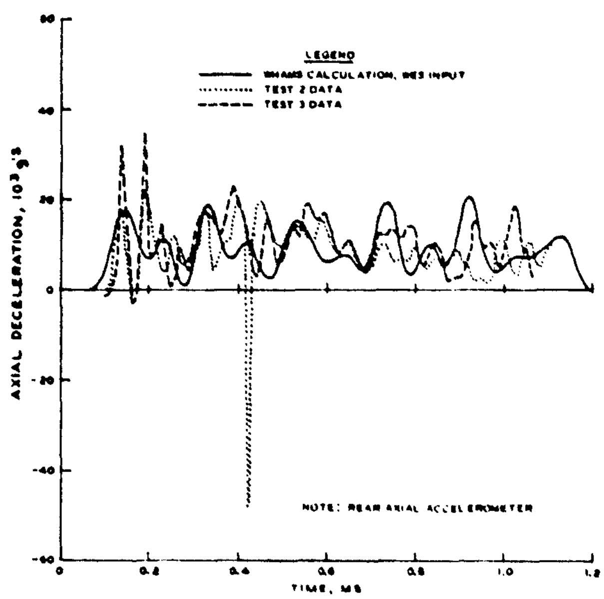

Figure 3.3 Comparison of calculated and measured axial decelerations for Sandia/DNA RBT, 3-degree attack angle.

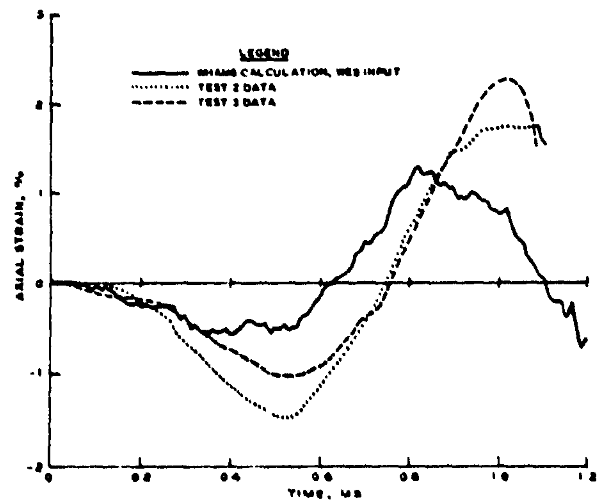

Figure 3.4 Comparison of calculated and measured strains for Sandia/DNA RBT, 3-degree attack angle.

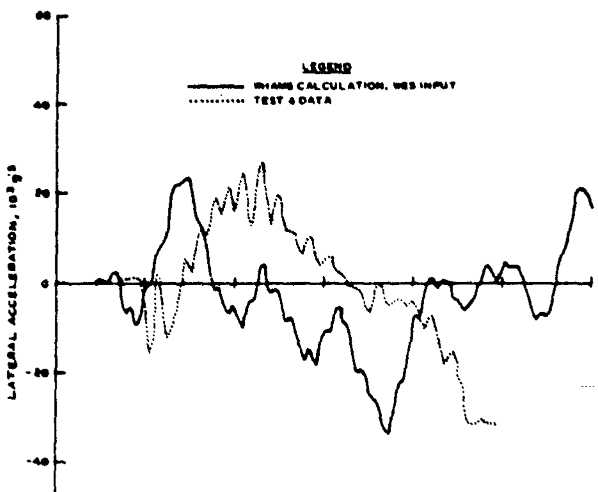

Figure 3.5 Comparison of calculated and measured lateral accelerations for Sandia/DNA RBT, 20-degree obliquity.

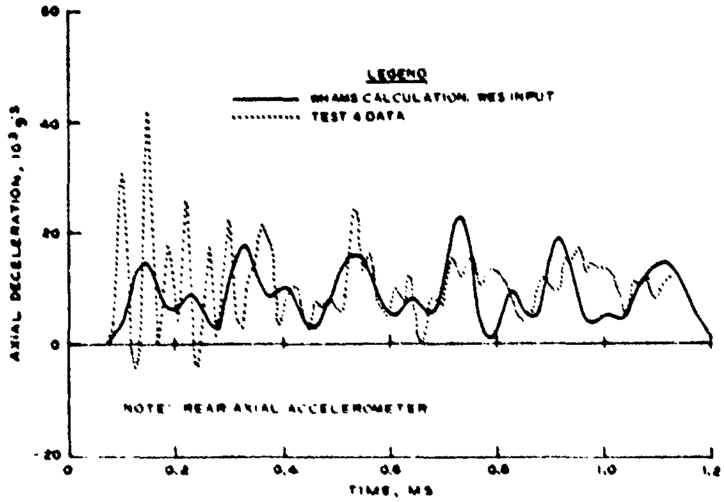

Figure 3.6 Comparison of calculated and measured axial decelerations for Sandia/DNA RBT, 20-degree obliquity.

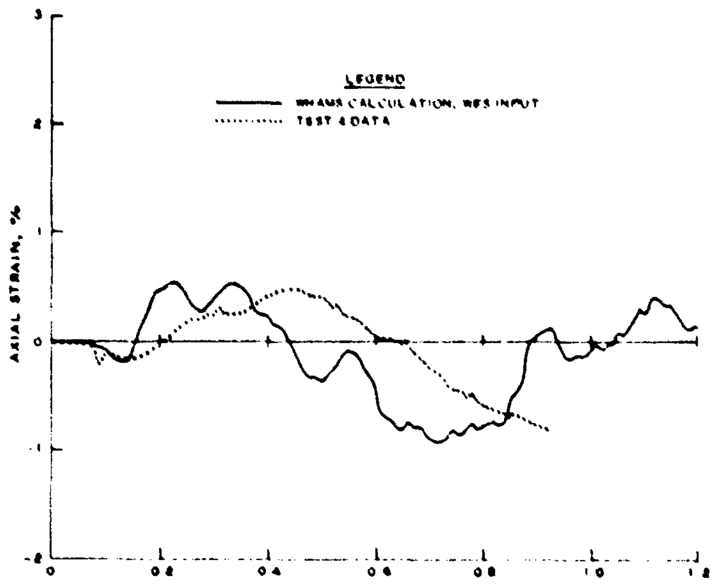

Figure 3.7 Comparison of calculated and measured strains for Sandia/DNA RBT, 20-degree obliquity.

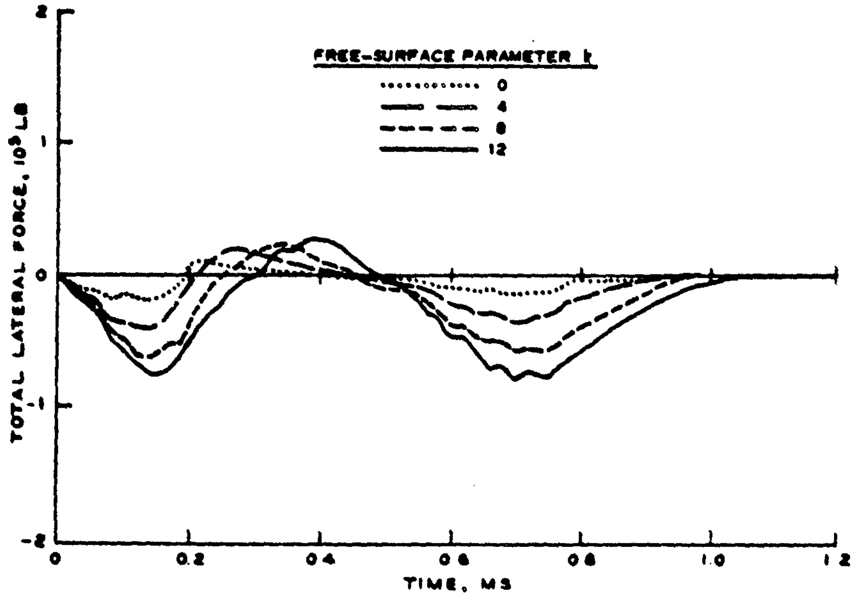

Figure 3.8 Calculated lateral force for different values of free-surface parameter, Sandia/DNA RBT, 20-degree obliquity.

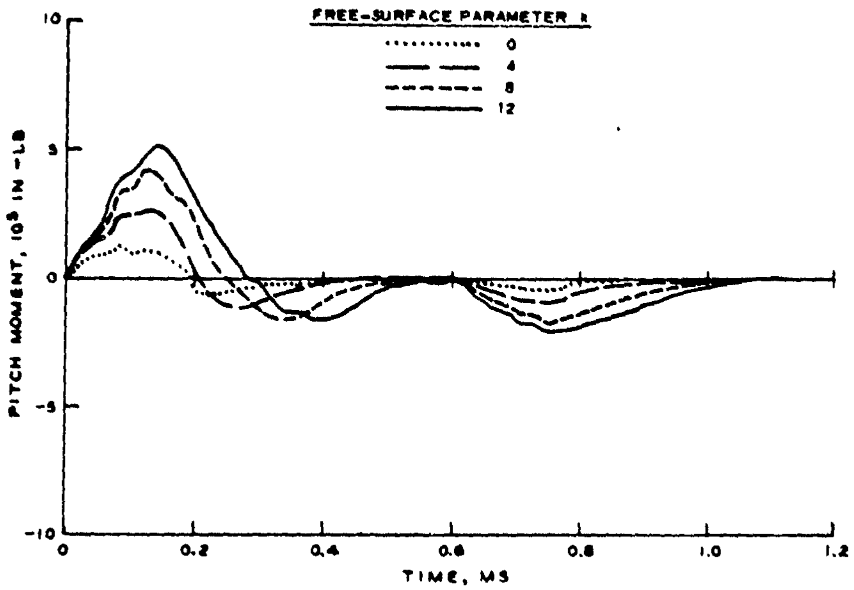

Figure 3.9 Calculated pitch moment for different values of free-surface parameter, Sandia/DNA RBT, 20-degree obliquity.

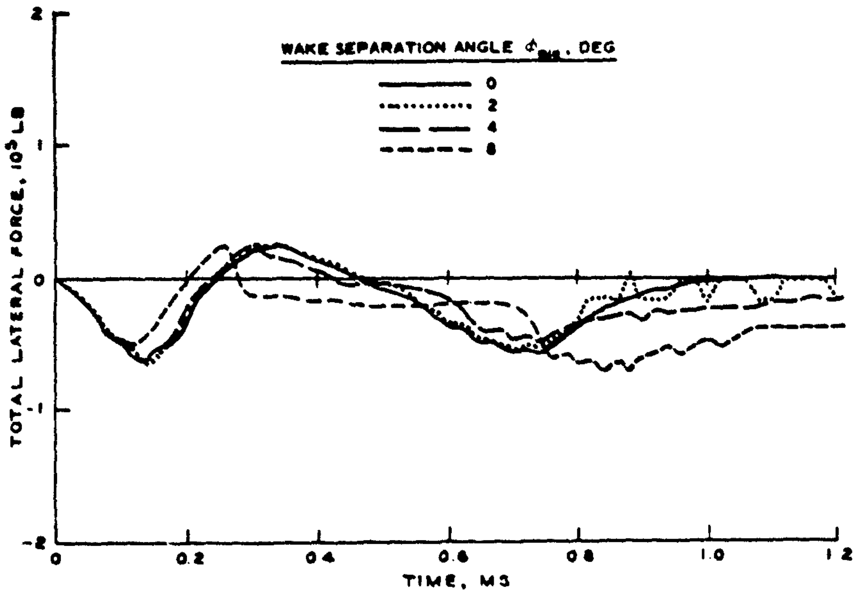

Figure 3.10 Calculated lateral force for different values of wake separation angle, Sandia/DNA RBT, 20-degree obliquity.

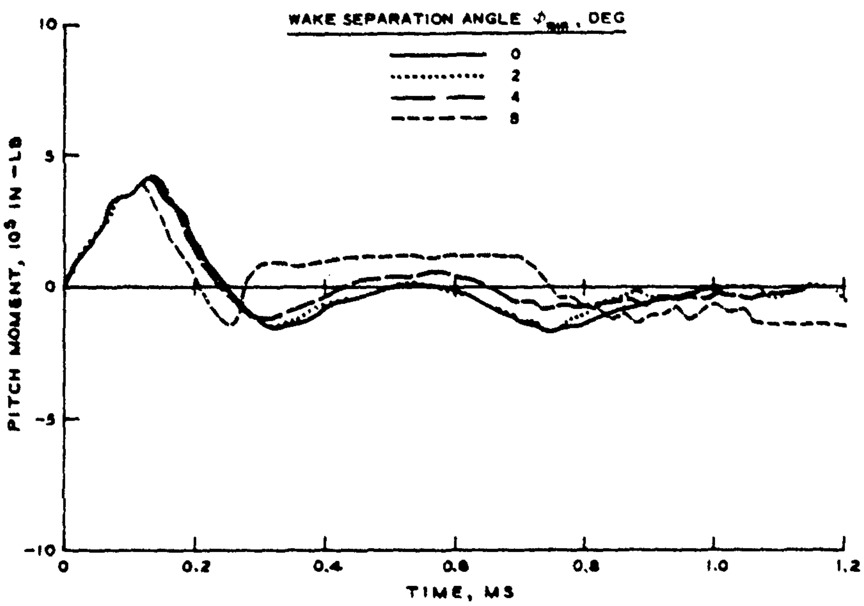

Figure 3.11 Calculated pitch moment for different values of wake separation angle, Sandia/DNA RBT, 20-degree obliquity.

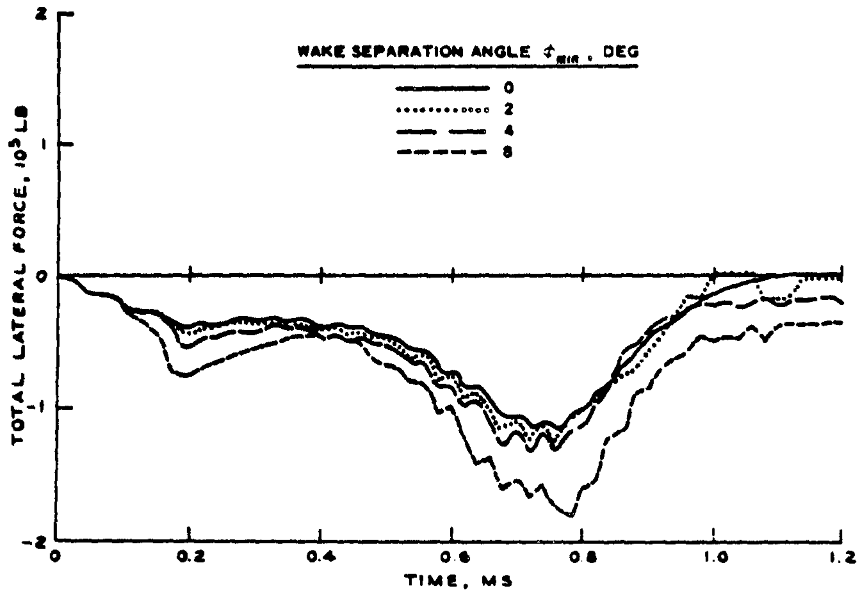

Figure 3.12 Calculated lateral force for different values of wake separation angle for Sandia/DNA RBT, 3-degree attack angle.

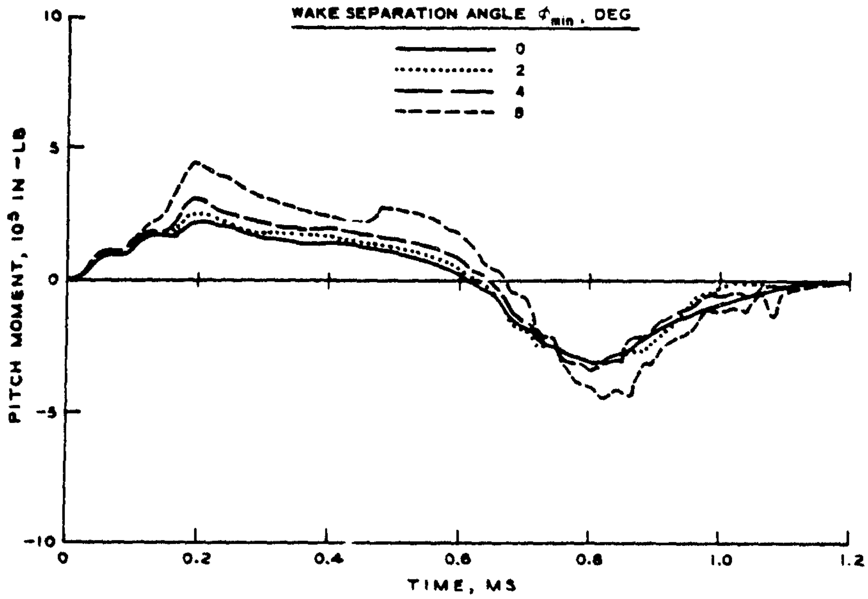

Figure 3.13 Calculated pitch moment for different values of wake separation angle for Sandia/DNA RBT, 3-degree attack angle.

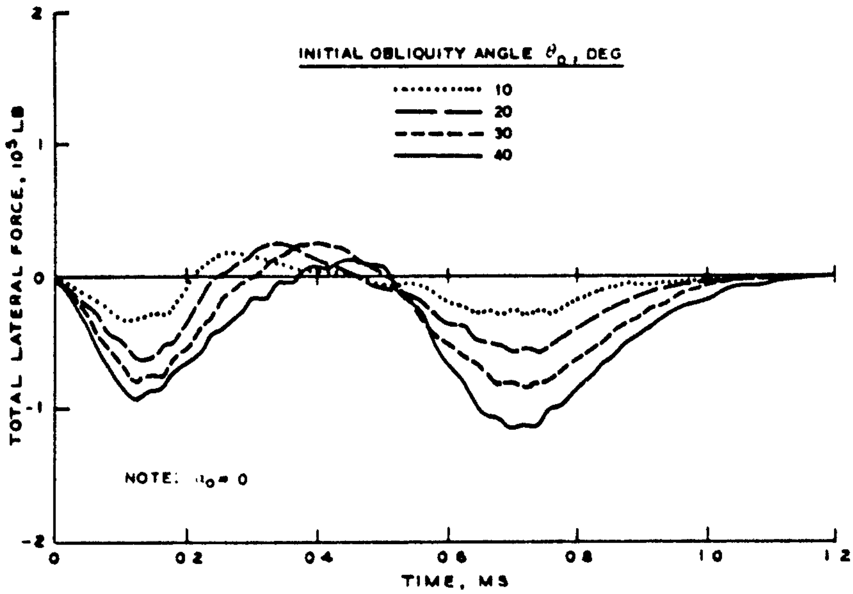

Figure 3.14 Calculated lateral force for different values of obliquity, Sandia/DNA RBT.

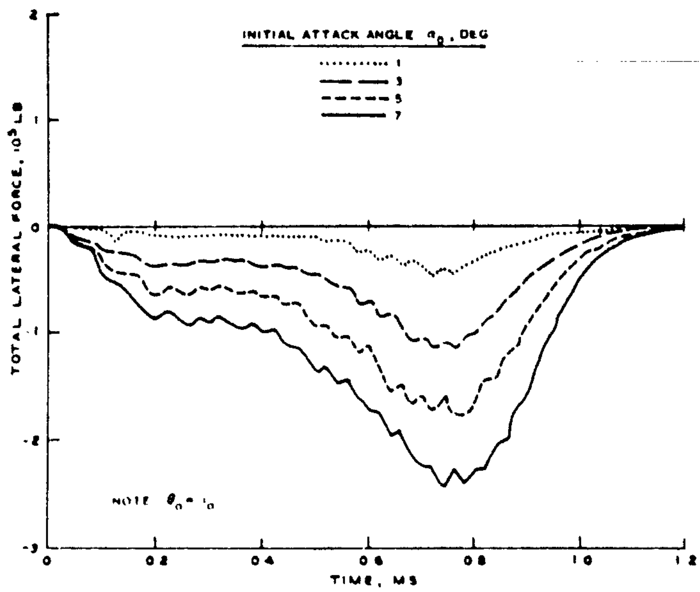

Figure 3.15 Calculated lateral force for different values of attack angle, Sandia/DNA RBT.

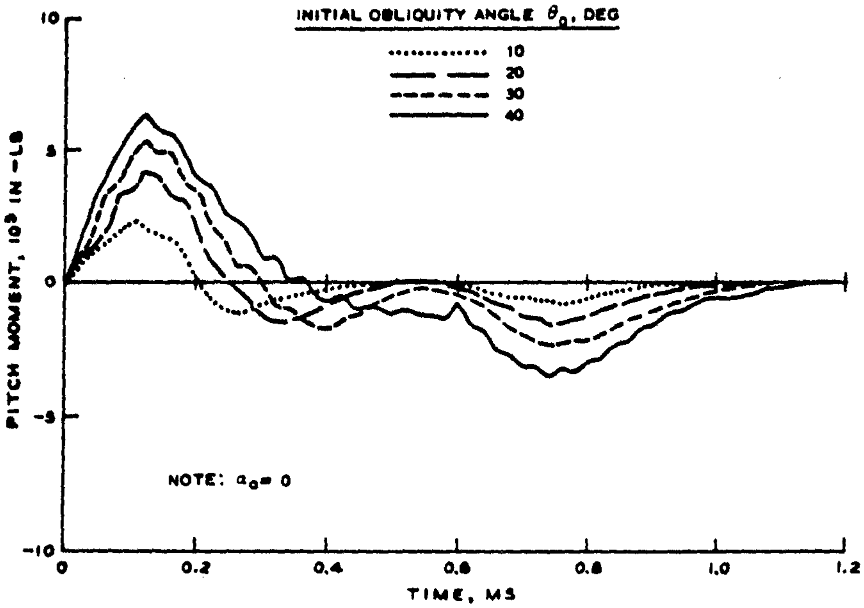

Figure 3.16 Calculated pitch moment for different values of obliquity, Sandia/DNA RBT.

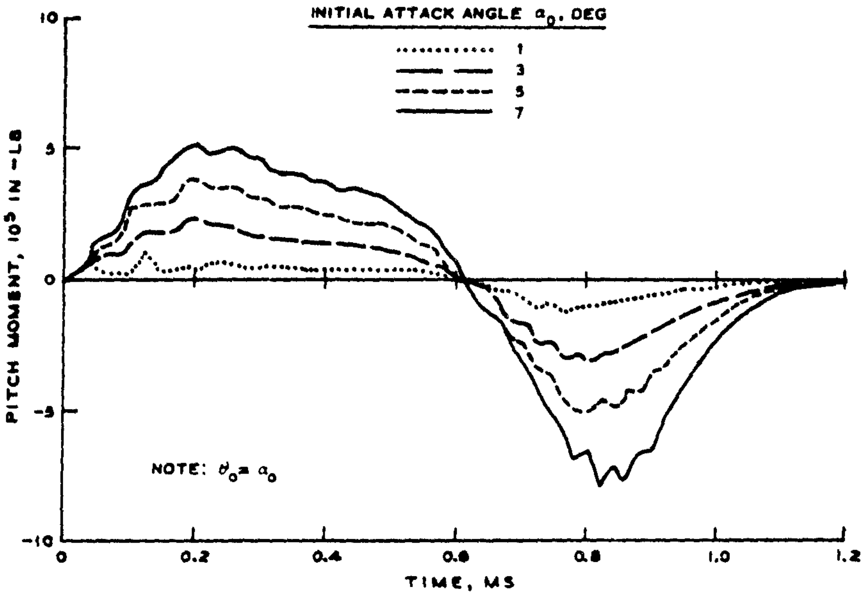

Figure 3.17 Calculated pitch moment for different values of attack angle, Sandia/DNA RBT.

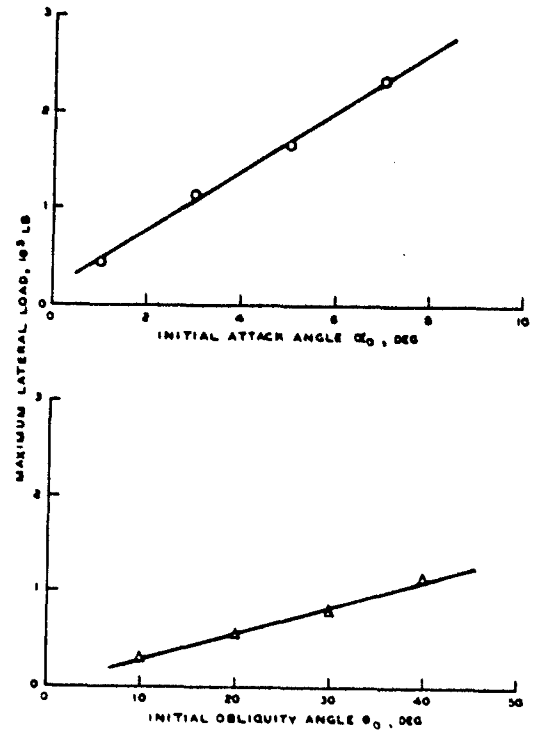

Figure 3.18 Variation of maximum calculated lateral load with attack angle and obliquity, Sandia/DNA RBT.

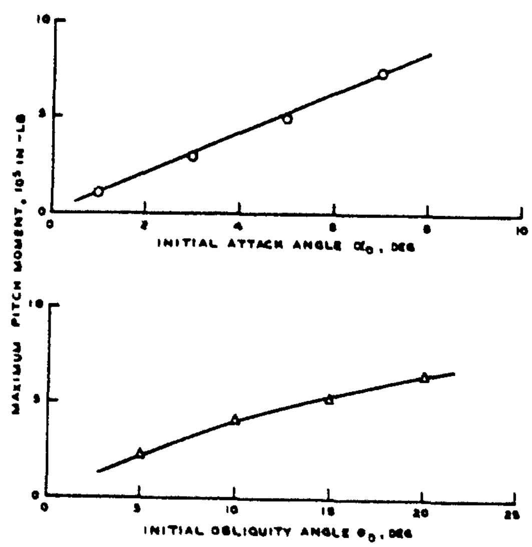

Figure 3.19 Variation of maximum calculated pitch moment with attack angle and obliquity, Sandia/DNA RBT.

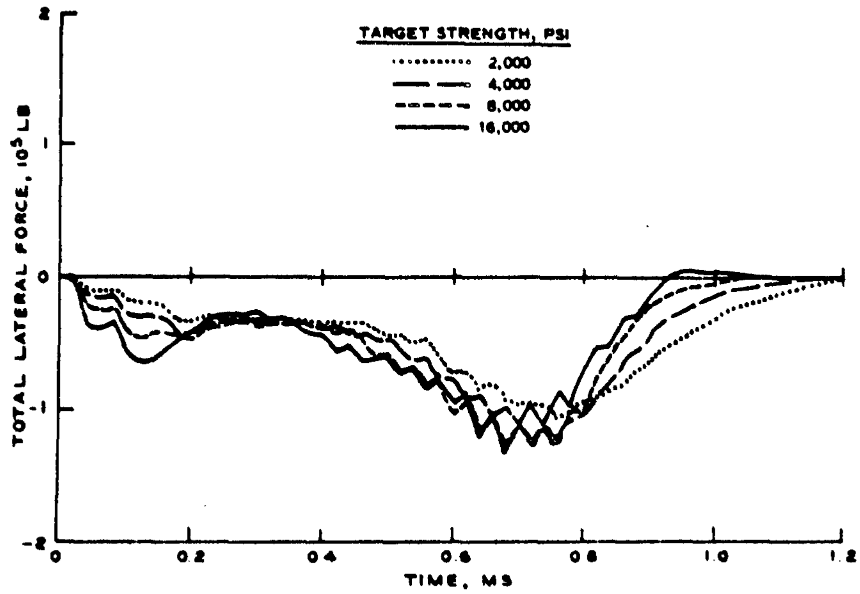

Figure 3.20 Calculated lateral force for different values of target strength, Sandia/DNA RBT, 3-degree attack angle.

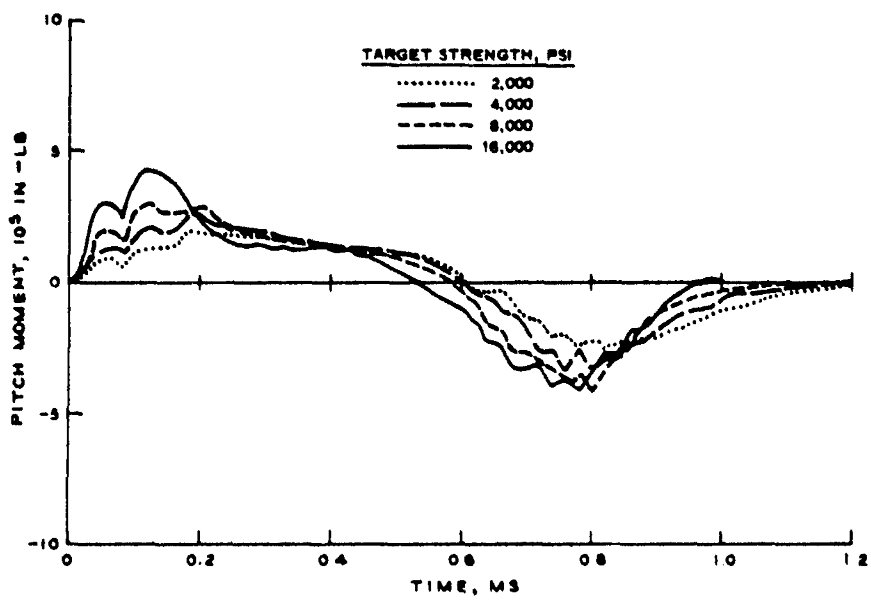

Figure 3.21 Calculated pitch moment for different values of target strength, Sandia/DNA RBT, 3-degree attack angle.

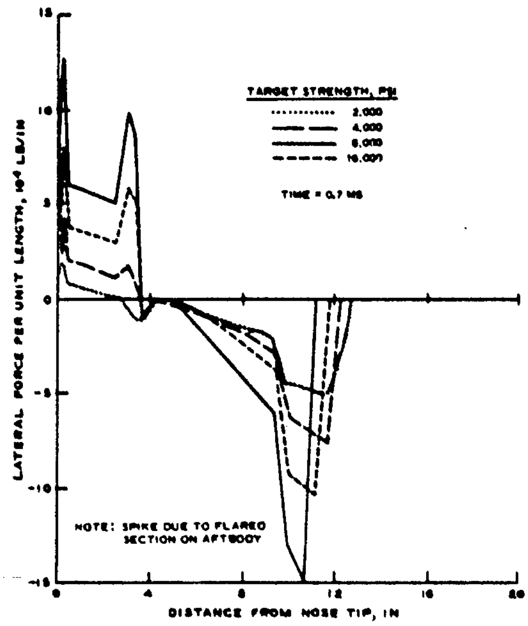

Figure 3.22 Calculated lateral force distribution for different values of target strength, Sandia/DNA RBT, 3-degree attack angle.

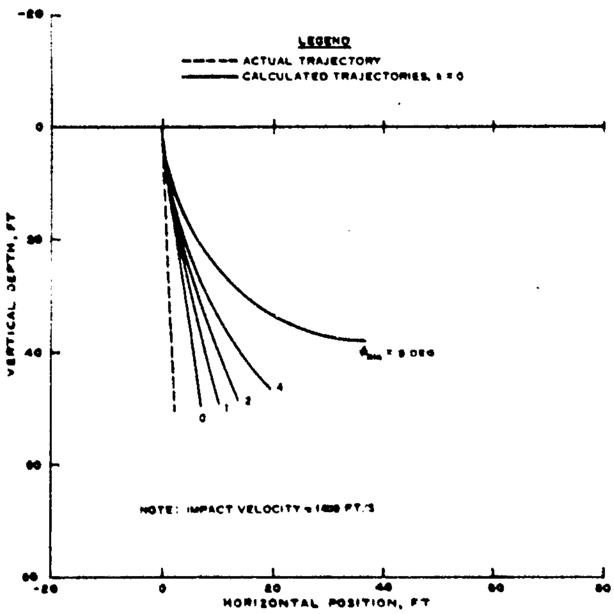

Figure 3.23 Effect of wake separation angle ϕ_{min} on calculated trajectories, Sandia Test R800915.

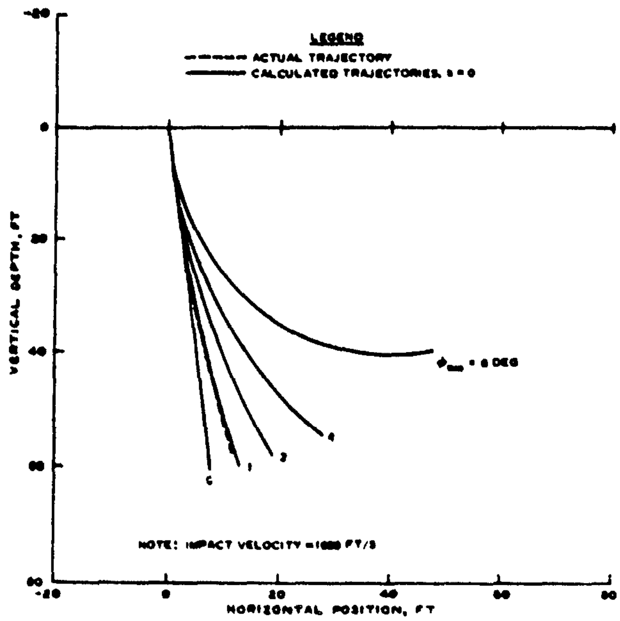

Figure 3.24 Effect of wake separation angle ϕ_{min} on calculated trajectories, Sandia Test R800916.

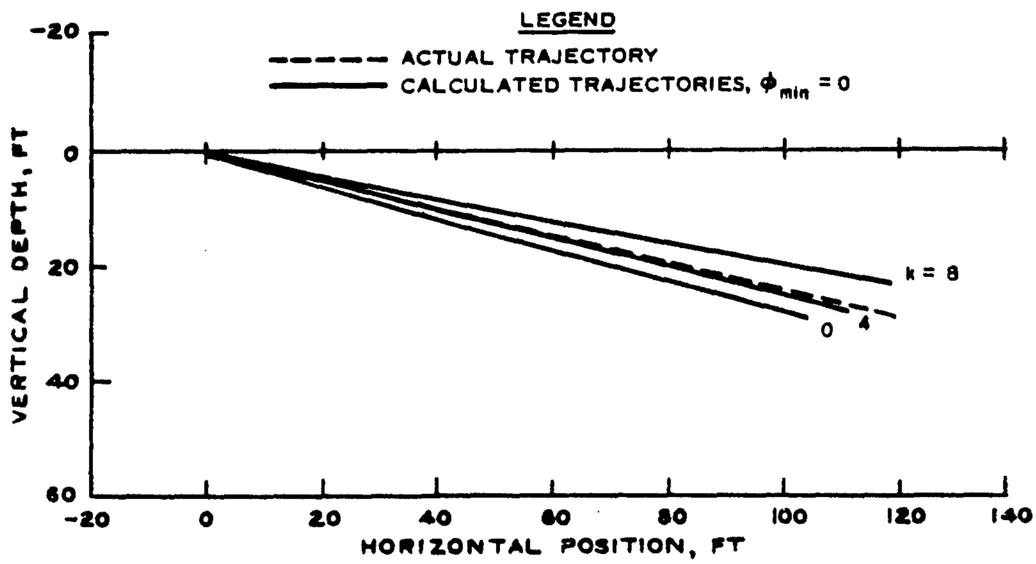

Figure 3.25 Effect of free-surface parameter k on calculated trajectories, Sandia Test R454025-23.

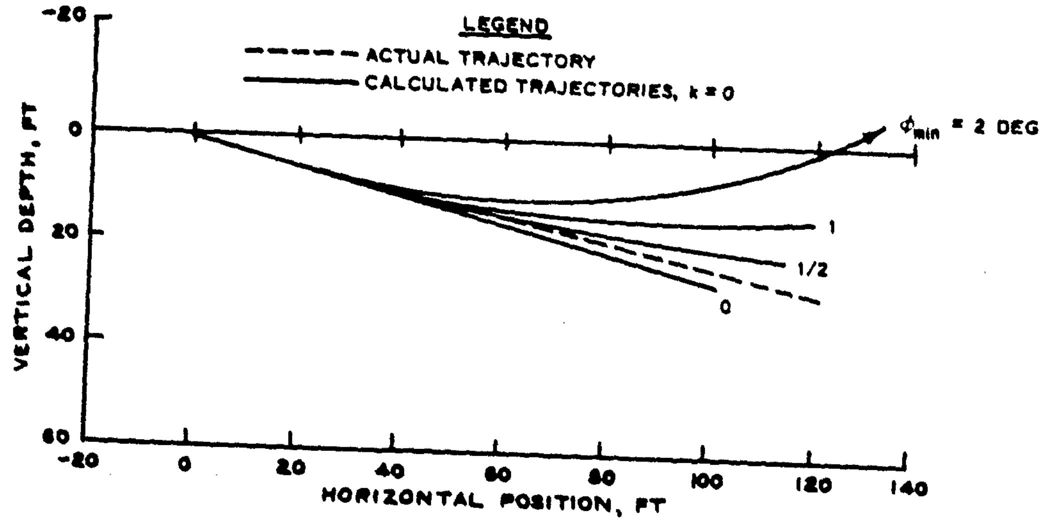

Figure 3.26 Effect of wake separation angle ϕ_{min} on calculated trajectories, Sandia Test R454025-23.

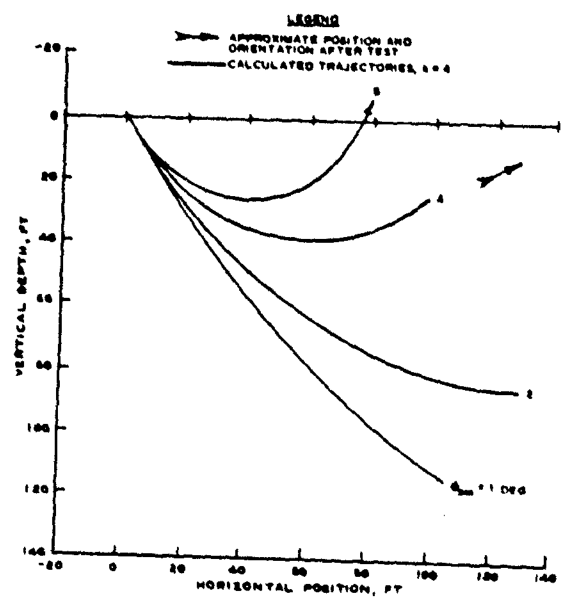

Figure 3.27 Effect of wake separation angle ϕ_{min} on calculated trajectories, Sandia Test R454025-22.

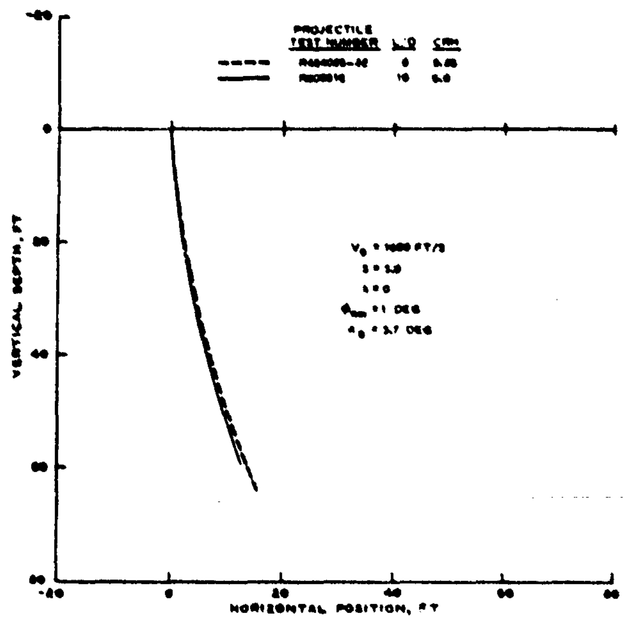

Figure 3.28 Comparison of calculated trajectories for Sandia penetrators, ϕ_{min} = 1 degree.

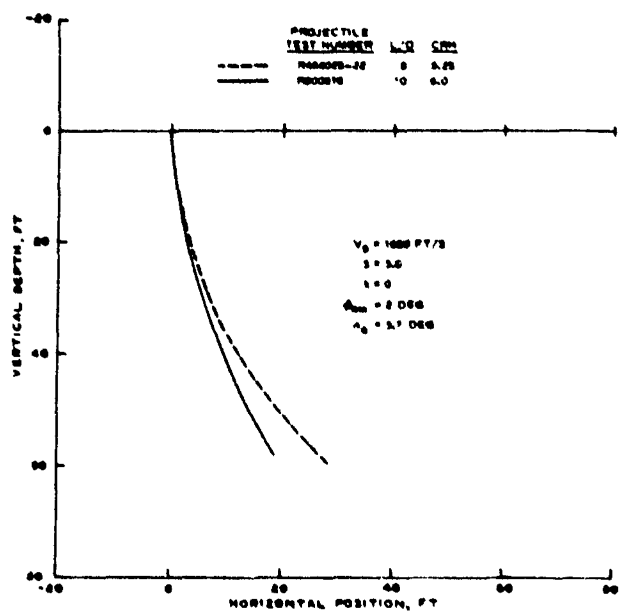

Figure 3.29 Comparison of calculated trajectories for Sandia penetrators, ϕ_{min} = 2 degrees.

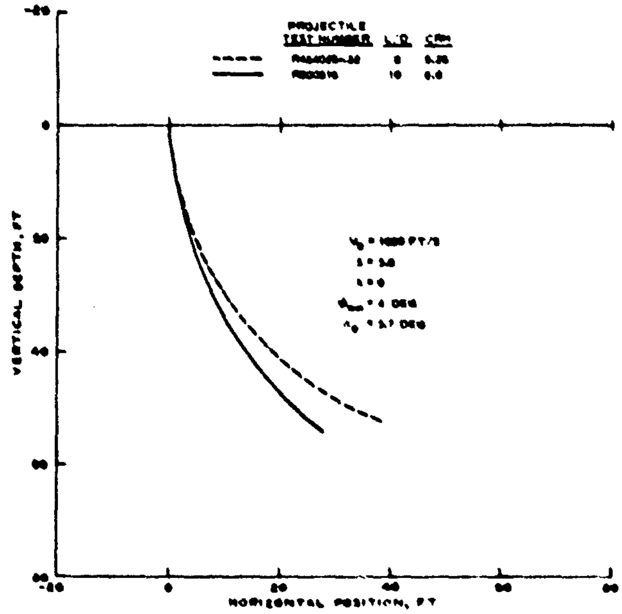

Figure 3.30 Comparison of calculated trajectories for Sandia penetrators, ϕ_{min} = 4 degrees.

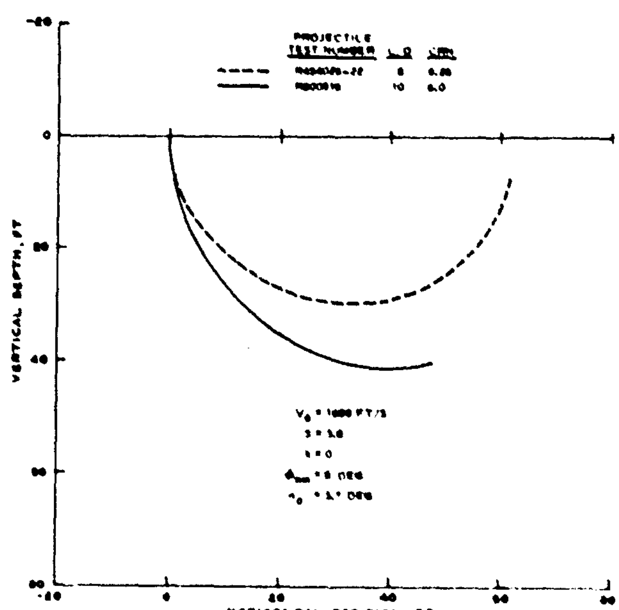

Figure 3.31 Comparison of calculated trajectories for Sandia penetrators, ϕ_{min} = 8 degrees.

CHAPTER 4

PARAMETER STUDY FOR SOIL PENETRATION

4.1 BACKGROUND

The PENCO2D computer code predicts trajectories that seem reasonable in light of existing non-normal soil penetration data (Chapter 3), although inconsistencies in the test results leave unresolved the question of wake separation and its quantitative effect on stability. Uncertainties notwithstanding, enough benchmarks do exist so that some credence can be given to a study of the effects of varying the projectile parameters, the impact conditions, and the target penetrability.

A baseline projectile, target, and set of impact conditions are specified in this chapter, and calculations are presented in which individual parameters have been varied one at a time. In some cases the variation of a given quantity independent of other quantities may be unrealistic in a practical sense (e.g., changing the projectile length without affecting the moment of inertia). However, the objective in such instances is to show the influence of a particular parameter in the calculation itself. In a practical design-parameter study (Section 4.6), coupled parameters (e.g., weight, length, and mass moment of inertia) have to be varied together.

4.2 BASELINE CONDITIONS

The projectile chosen for this study is similar to the one used in Sandia Test R454025-23 (L/D = 8) and represents a marginally stable design, according to Sandia's experience. The pertinent projectile quantities are

$$W = 300 \text{ lb}$$

$$D = 6 \text{ in}$$

$$L = 48 \text{ in}$$

$$CRH = 6.0$$

$$\text{CG location} \quad \zeta_{CG} = 26.4 \text{ in from nose tip}$$

$$I = 4 \times 10^4 \text{ lb-in}^2$$

$$\text{Aftbody taper angle} \quad \phi_{aft} = 0$$

The baseline impact conditions are

$$V_o = 1500 \text{ ft/sec}$$

$$\alpha_o = 4 \text{ degrees}$$

$$\theta_o = 4 \text{ degrees}$$

The baseline target properties are

$$S = 8$$

$$k = 4$$

$$\phi_{min} = 2 \text{ degrees}$$

All of the above parameters will be varied except k and ϕ_{min}, whose effects have already been demonstrated in Chapter 3. Aside from the individual quantity or quantities being varied, the input will be the same as the baseline conditions.[1]

Figures 4.1, 4.2, and 4.3 show the trajectory, external forces, and pitch moment, respectively, calculated for the baseline conditions. Since the baseline calculation uses a constant wake separation angle (ϕ_{min} = 2 degrees), the penetration path is curved, rather than straight, and there is some residual oscillation in the pitch moment as aftbody contact alternately increases and decreases.

4.3 VARIATION OF TARGET PENETRABILITY AND IMPACT CONDITIONS

Figure 4.4 indicates the degree to which the target S-number influences the trajectory. The main effect seems to be an increase in the total path length with increasing S. Although the horizontal displacement increases with S, there seems to be little variation in the

---

[1] The baseline calculation will appear in all comparisons of trajectories <u>except</u> Figure 4.7, and will be represented by a solid curve (e.g., Figure 4.1).

overall path shape. The same thing can be said for the impact velocity (Figure 4.5).

The initial attack angle has a mild effect on the trajectory (Figure 4.6), aside from a marked increase in path curvature and horizontal displacement between 0 and 2 degrees. The 0-degree case goes straight in because there is no angle of attack (or obliquity) to initiate rotation. Large obliquities ($\alpha_o = 0$, $\theta_o \geq 60$ degrees) can produce ricochet (Figure 4.7), although lesser obliquities seem to have a gentle effect on path curvature.[2]

4.4 INDEPENDENT VARIATION OF PROJECTILE PARAMETERS FOR STRAIGHT AFTBODY

Figures 4.8, 4.9, and 4.10 show the effects of varying the weight, diameter, and nose shape, respectively. Treated as independent parameters, none of these variables has much effect other than changing the path length. The horizontal displacement increases with path length, but the shape of the trajectory changes only slightly.

It might be argued that the mass moment of inertia alone should have a big influence on the trajectory. This is not the case, however, as can be seen in Figure 4.11. Although the mass moment of inertia has a moderately stabilizing effect, it is overshadowed by aftbody separation, which allows the projectile to rotate with little opposition during most of the event (see Figure 4.3).

Figure 4.12 shows the consequences of treating the projectile length as an <u>independent</u> parameter, keeping the geometric position of the CG constant ($\zeta_{CG}/L = 0.55$). A reduction in projectile length has a stabilizing effect, due to reductions in the moment arm and the total (lateral) loaded area on either side of the CG. This is the least realistic of all the foregoing trajectory comparisons because a physical change in length changes <u>all</u> other parameters (Section 4.6).

The most important single parameter is the geometric CG location

---

[2] The initial obliquity required for ricochet would be smaller if a larger value has been chosen for ϕ_{min}

ζ_{CG}/L , as is indicated in Figure 4.13. If the CG is far enough forward ($\zeta_{CG}/L = 0.45$), the negative moment (after CG entry into the target) outweighs the initial positive moment, and a rotation reversal occurs. If the CG is far enough aft ($\zeta_{CG}/L = 0.65$), the initial positive moment is so great that the projectile ends up going sideways.

4.5 VARIATION OF AFTBODY FLARE

Figure 4.14 shows trajectories calculated for different values of the aftbody flare angle ϕ_{aft} . In each calculation the aftbody merges with the ogive nose section at the point of tangency, where $\eta = \phi_{aft}$. An illustration for $\phi_{aft} = 3$ degrees is shown in Figure 4.15.

If $\phi_{aft} = \phi_{min}$, there is no loss of contact with the target, and the penetrator goes almost straight in. On the other hand, if $0 < \phi_{aft} < \phi_{min}$, the trajectory is straighter than the baseline case (straight aftbody, $\phi_{aft} = 0$) but it is still noticeably curved. Flare angles greater than ϕ_{min} reduce the final depth, due to increased base diameter (decreased W/A).

From this comparison, the optimum flare angle appears to be a value less than the wake separation angle, producing a slightly curved trajectory but leaving the depth essentially unaffected. The flare must be installed without shifting the CG toward the tail.

4.6 VARIATION OF COUPLED PROJECTILE PARAMETERS

The projectile parameters that were varied independently in Section 4.4 are coupled to one another in practice. As far as stability is concerned, the most important coupling occurs among weight, length, CG location, and mass moment of inertia. A serious parameter study should consider the simultaneous variation of these quantities.

A simple but fairly realistic way of accounting for the change in W , ζ_{CG} , and I with L is to add or subtract cylindrical aftbody sections of constant linear density[3] from the baseline projectile, while

[3] Constant weight/unit length = 300 lb/48 in = 6.25 lb/in.

assuming $I = ML^2$. Figure 4.16 shows trajectories for projectiles whose properties were varied in this way.

According to the calculations, if the projectile is short enougn ($L/D < 5$), the CG will lie in an unstable position, ultimately producing sideways motion.[4] Otherwise, the effect of the changing parameters is little more than an increase in path length with projectile length.

---

[4] See also Figure 4.13.

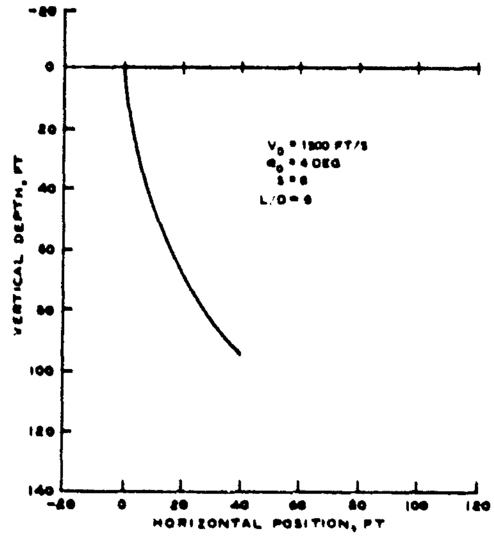

Figure 4.1 Calculated trajectory for baseline conditions.

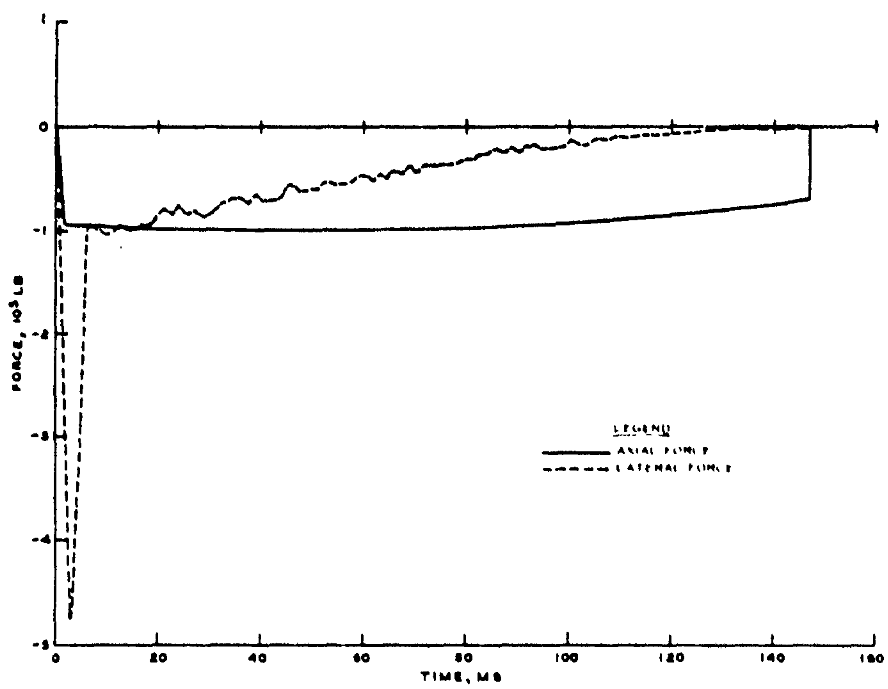

Figure 4.2 Calculated external forces for baseline conditions.

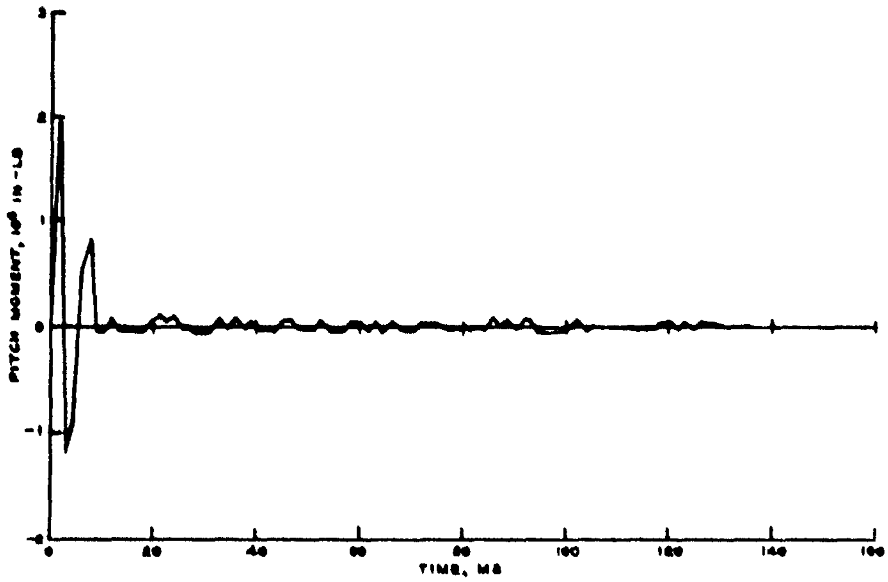

Figure 4.3 Calculated pitch moment for baseline conditions.

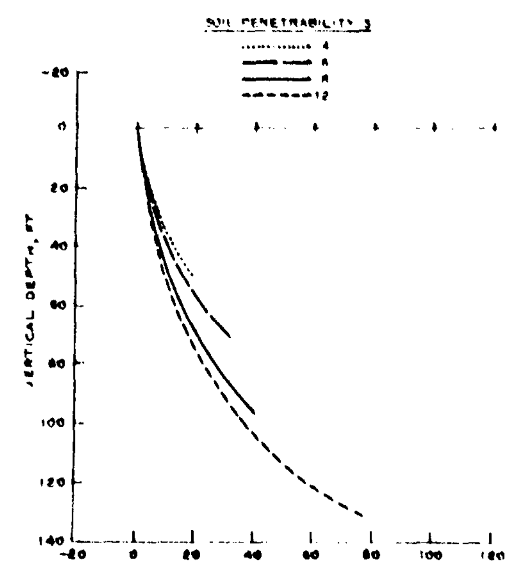

Figure 4.4 Effect of soil penetrability on calculated trajectories.

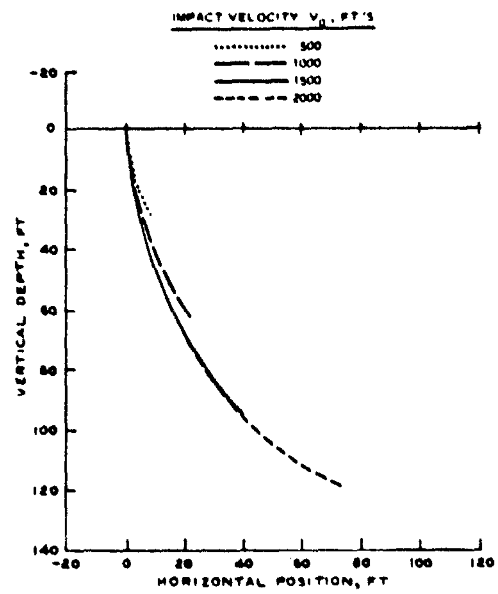

Figure 4.5 Effect of impact velocity on calculated trajectories.

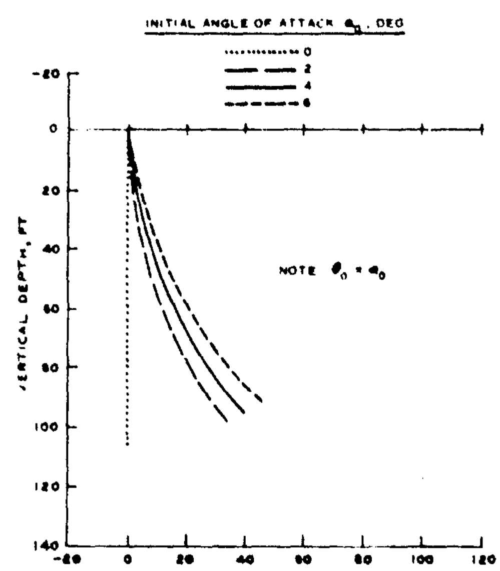

Figure 4.6 Effect of attack angle on calculated trajectories.

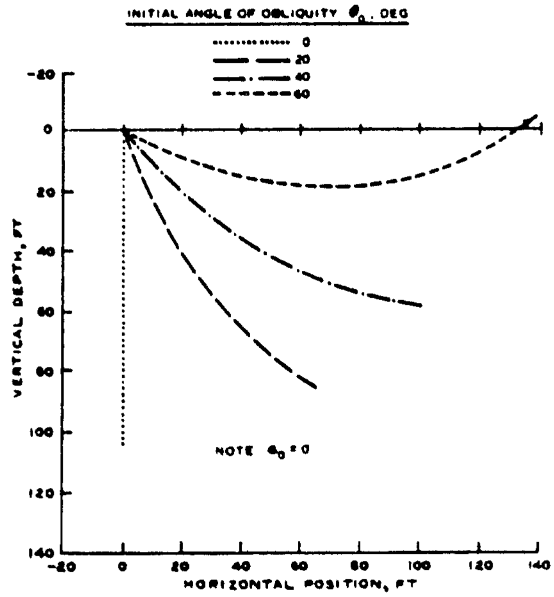

Figure 4.7 Effect of obliquity on calculated trajectories.

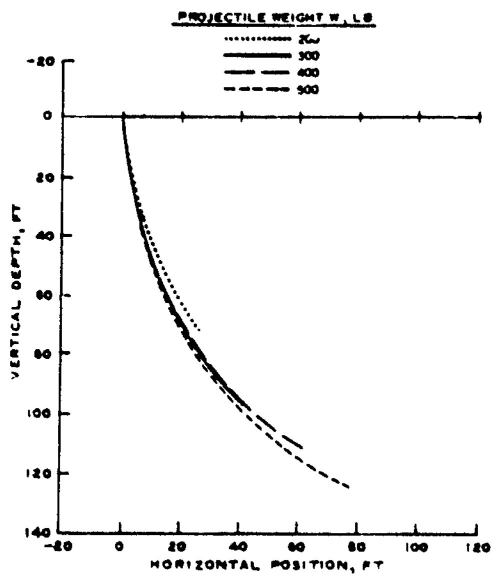

Figure 4.8 Effect of projectile weight on calculated trajectories.

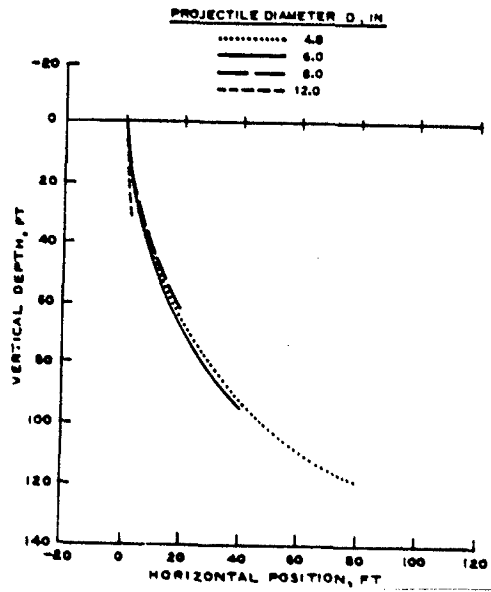

Figure 4.9 Effect of projectile diameter on calculated trajectories.

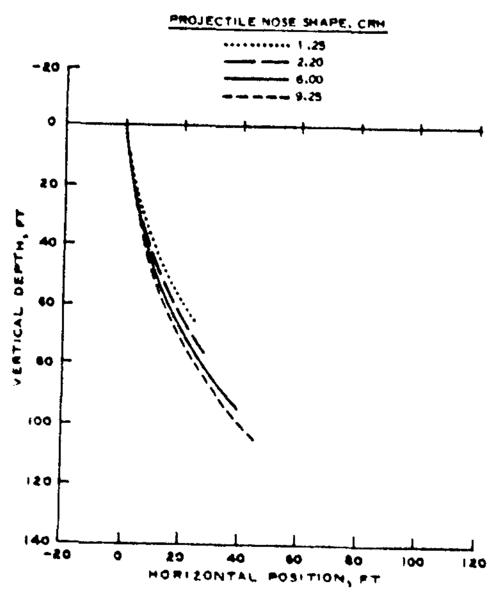

Figure 4.10 Effect of projectile nose shape on calculated trajectories.

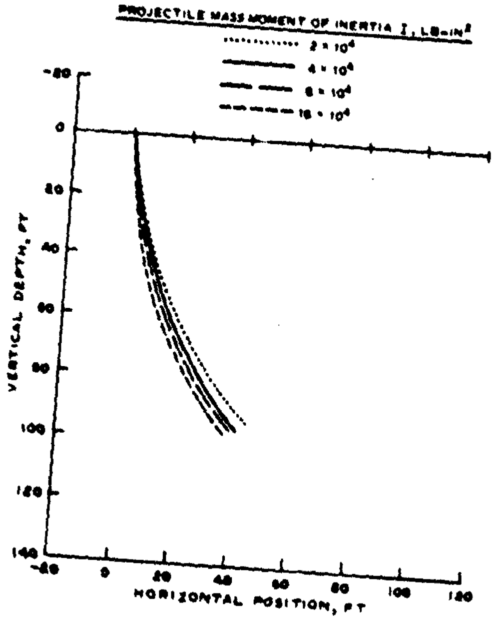

Figure 4.11 Effect of projectile mass moment of inertia on calculated trajectories.

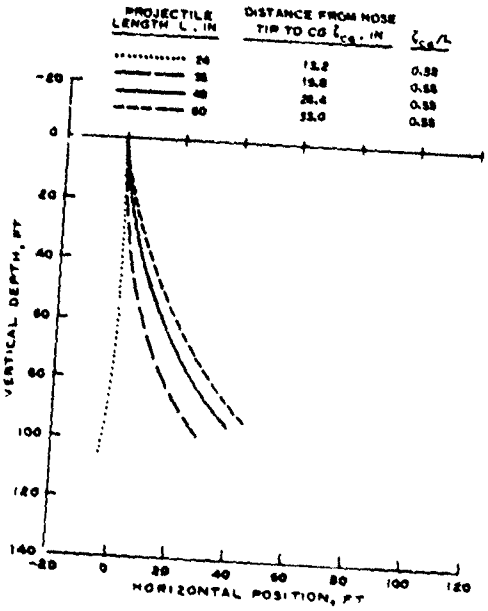

Figure 4.12 Effect of projectile length (as an independent parameter) on calculated trajectories.

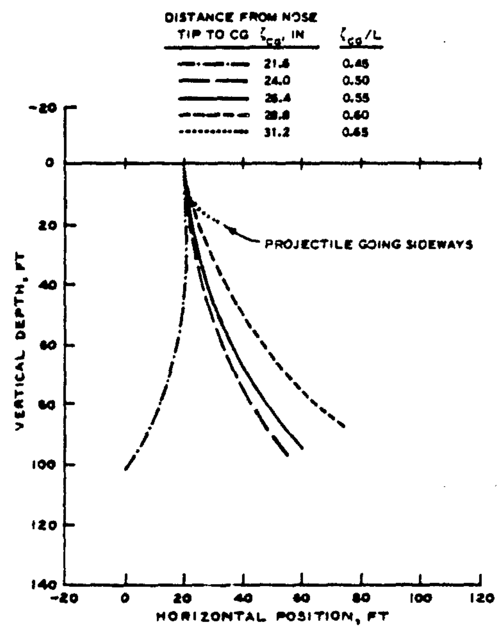

Figure 4.13 Effect of CG location on calculated trajectories.

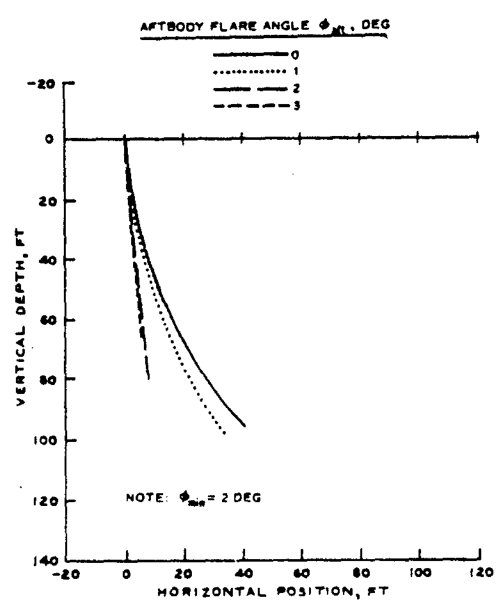

Figure 4.14 Effect of aftbody flare on calculated trajectories.

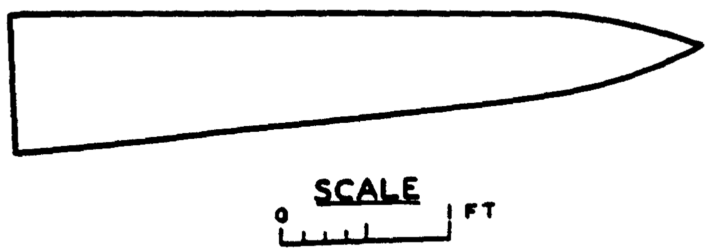

Figure 4.15 Scale drawing of projectile with 3-degree aftbody flare

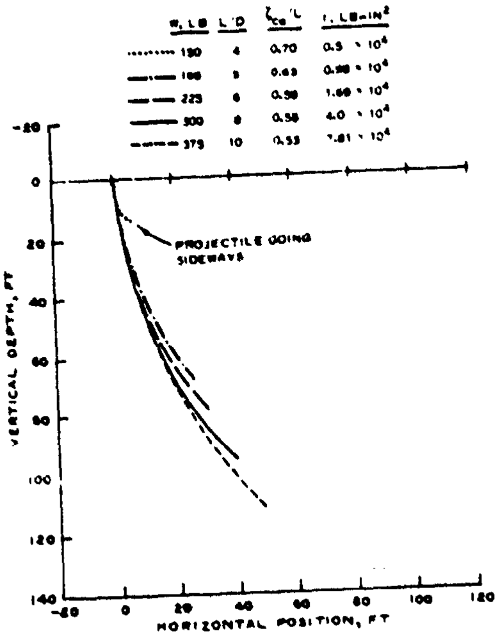

Figure 4.16 Combined effects of weight, length, CG location, and mass moment of inertia on calculated trajectories.

CHAPTER 5

CONCLUSIONS

An empirical theory has been developed for analyzing impact and penetration in soil and rock. Calculations with this theory reproduce penetration data for normal impact at least as well as other empirical analyses (e.g., Young's equation). The extension from one- to two-dimensional motion was obtained by extrapolation, with simple models postulated for the free-surface and wake separation effects. The entire non-normal analysis was then incorporated into the PENCO2D computer code. Benchmarks for the theory consist of strain and acceleration data from RBT's in sandstone, and trajectory data from conventional penetration tests into soil.

Projectile acceleration and strain predictions,[1] generated from WES-calculated external loads, agree fairly well with the RBT data. There is, however, a tendency to underpredict the lateral loads for yawed impact somewhat. There is also an unexplained phase difference between the calculated and observed lateral accelerations for both yawed and non-yawed oblique impact. On the other hand, the calculated variations of maximum lateral force and pitch moment with initial obliquity and attack angle are quite reasonable (essentially linear). In any case, the recommended values for the wake separation angle and free-surface parameter, respectively, are $\phi_{min} = 0$ and $k = 8$ for rock and rocklike materials.[2]

Comparisons of calculated and observed penetrator trajectories in soil are inconclusive, since the test data are not consistent. Concerning terradynamic stability, however, the most important target parameter is the wake separation angle,[3] whereas the most important projectile

---

[1] WHAMS code (dynamic structural response) calculations made by T. Belytschko, with PENCO2D calculations as input.

[2] These values gave reasonable external load predictions for the RBT's.

[3] At this point, it is impossible to specify the most likely values of the free-surface parameter and the wake separation angle. A reasonable guess for the respective ranges of values, however, is $0 \leq k < 8$ and $0 \leq \phi_{min} < 8$ degrees .

parameter is the CG location.[4] Aftbody flare also has a beneficial effect, if the CG is not shifted toward the tail and the base diameter is not increased enough to significantly reduce the final depth.

One phenomenon not predicted by the present theory is the marked improvement in projectile stability achieved by going from $L/D = 8$ to $L/D = 10$, which was observed in tests conducted by Sandia Laboratories (Reference 14). WES calculations indicate a gradual improvement in stability with projectile length (see Figure 4.16). If $L/D \approx 8$ does represent a critical value for projectile stability, this would indicate that some basic mechanism is missing in the theory, either in the wake separation analysis or in the stress equations.

One mechanism conspicuously absent in the present wake separation analysis is the resistance of the target to the (cylindrical) expansion of the wake cavity, which would lead ultimately to the rebound/collapse of the cavity on the aftbody. The probable variation of ϕ_{min} with velocity, depth, nose shape, and target penetrability (S-number) is also neglected. Finally, the stress equations may be underpredicting the effects of lateral motion. Future work should consider these problems and any others that might bear on the stability question.

[4] The latter conclusion was also drawn from the preliminary analysis (Reference 8).

REFERENCES

1. C. W. Young; "The Development of Empirical Equations for Predicting Depth of an Earth-Penetrating Projectile"; Development Report No. SC-DR-67-60, May 1967; Sandia Laboratories, Albuquerque, N. M.

2. C. W. Young; "Depth Prediction for Earth-Penetrating Projectiles"; Journal, Soil Mechanics and Foundations Division, American Society of Civil Engineers, Vol 95, No. SM3, May 1969; pp 803-817.

3. C. W. Young; "Empirical Equations for Predicting Penetration Performance in Layered Earth Materials for Complex Penetrator Configurations"; Development Report No. SC-DR-72-0523, Dec 1972; Sandia Laboratories, Albuquerque, N. M.

4. R. S. Bernard; "Depth and Motion Prediction for Earth Penetrators"; Technical Report S-78-4, Jun 1978; U. S. Army Engineer Waterways Experiment Station, CE, Vicksburg, Miss.

5. R. S. Bernard and D. C. Creighton; "Non-Normal Impact and Penetration: Analysis for Hard Targets and Small Angles of Attack"; Technical Report S-78-14, Sep 1978; U. S. Army Engineer Waterways Experiment Station, CE, Vicksburg, Miss.

6. Y. M. Ito and others; "Analysis of 0.284-Scale RBT for 3° Yawed Impact"; Informal Report, Contract DNA 001-76-C-0383, Oct 1978; California Research and Technology, Inc., Woodland Hills, Calif.

7. D. Henderson and E. J. Giara, Jr.; "Earth Penetrator Technology Program"; Draft Report DNA 4571, Jan 1978; Avco Systems Division, Wilmington, Mass.

8. R. S. Bernard; "Earth-Penetrator Trajectories in Soil: Preliminary Analysis and Parameter Study"; Letter Report to Defense Nuclear Agency, Oct 1978; U. S. Army Engineer Waterways Experiment Station, CE, Vicksburg, Miss.

9. C. W. Livingston and F. L. Smith; "Bomb Penetration Project"; Apr 1951; Colorado School of Mines and Research Foundation, Inc., Golden, Colo.

10. W. R. Kampfe; "DNA 1/3-Scale Pershing Penetrator Tests"; Letter Report to Defense Nuclear Agency dated Oct 1977; Sandia Laboratories, Albuquerque, N. M.

11. D. C. Creighton; "Correlation of Reverse Ballistic Test Data"; Letter Report to Defense Nuclear Agency, Dec 1977; U. S. Army Engineer Waterways Experiment Station, CE, Vicksburg, Miss.

12. D. C. Creighton; "Correlation of Additional Reverse Ballistic Test Data"; Letter Report to Defense Nuclear Agency, Aug 1978; U. S. Army Engineer Waterways Experiment Station, CE, Vicksburg, Miss.

13. C. W. Young; "Results of December 1977 Davis Gun Tests at TTR"; Memorandum dated 13 Jan 1978; Sandia Laboratories, Albuquerque, N. M.

14. C. W. Young; "Status Report on High Velocity Penetration Program"; Report No. SAND 76-0291, Sep 1976; Sandia Laboratories, Albuquerque, N. M.

15. R. S. Bernard and S. V. Hanagud; "Development of a Projectile Penetration Theory, Report 1"; Technical Report S-75-9, Jun 1975; U. S. Army Engineer Waterways Experiment Station, CE, Vicksburg, Miss.

16. R. S. Bernard; "Development of a Projectile Penetration Theory, Report 2"; Technical Report S-75-9, Feb 1976; U. S. Army Engineer Waterways Experiment Station, CE, Vicksburg, Miss.

17. R. S. Bernard and D. C. Creighton; "Projectile Penetration in Earth Materials: Theory and Computer Analysis"; Technical Report S-76-13, Nov 1976; U. S. Army Engineer Waterways Experiment Station, CE, Vicksburg, Miss.

18. J. A. Canfield and I. G. Clator; "Development of a Scaling Law and Techniques to Investigate Penetration in Concrete"; Technical Report 2057, Aug 1966; U. S. Naval Weapons Laboratory, Dahlgren, Va.

19. W. J. Patterson, Sandia Laboratories, Albuquerque, N. M., Untitled Letter Report to: R. S. Bernard, Soil Dynamics Division, U. S. Army Engineer Waterways Experiment Station, CE, Vicksburg, Miss.; 26 Aug 1976.

20. D. U. Deere; "Technical Description of Rock Cores for Engineering Purposes"; Rock Mechanics and Engineering Geology, 1964, Vol. 1, No. 1, pp 16-22; International Society of Rock Mechanics, Springer-Verlag, N. Y.

21. D. J. Dunn; "Bomb Penetration of Earth-Covered Concrete Targets"; Proceedings of the Seminar on the Attack of Earth, Stone, and Concrete Barriers by HE Projectiles (15-16 May 1974), Part 1, Report BRL-R-1872, Apr 1976; U. S. Ballistic Research Laboratories, Aberdeen Proving Ground, Md.

22. R. S. Bernard; "Empirical Analysis of Projectile Penetration in Rock"; Miscellaneous Paper S-77-16, Nov 1977; U. S. Army Engineer Waterways Experiment Station, CE, Vicksburg, Miss.

23. W. J. Patterson; "Projectile Penetration of In Situ Pock"; Report No. SLA-73-9831, Nov 1973; Sandia Laboratories, Albuquerque, N. M.

24. S. W. Butters and others; "Field, Laboratory and Modeling Studies on Mount Helen Welded Tuff for Earth Penetrator Test Evaluation"; Report No. TR 75-9, Aug 1976; Terra Tek, Inc., Salt Lake City, Utah.

25. D. K. Butler and others; "Constitutive Property Investigations in Support of Full-Scale Penetration Tests in Dakota Sandstone, San Ysidro, New Mexico"; Technical Report S-77-3, Apr 1977; U. S. Army Engineer Waterways Experiment Station, CE, Vicksburg, Miss.

26. W. J. Patterson; "Physical Properties and Classification of Seven Types of Rock Targets"; Report No. SC-TM-68-621, Sep 1968; Sandia Laboratories, Albuquerque, N. M.

27. C. W. Young and G. M. Ozanne; "Compilation of Low Velocity Penetration Data"; Report No. SC-RR-306A, Jun 1966; Sandia Laboratories, Albuquerque, N. M.

APPENDIX A

PENETRATION THEORY FOR ROCK AND CONCRETE

A.1 EMPIRICAL THEORY FOR NORMAL IMPACT

Early penetration analyses at WES (References 15 through 17) relied heavily on the Cavity Expansion Theory (CET), whereby the coefficients a and b and the function $f(V)$ in the resisting stress

$$\sigma = a + b\,f(V) \tag{A.1}$$

could be obtained explicitly in terms of the density, strength, and elastic moduli of the target. Examination of penetration data from several sources, however, has failed to show a consistent correlation between penetrability and standard engineering properties, especially for soil. Although the most consistently accurate predictions have been obtained for concrete, additional factors such as aggregate size may overshadow elastic effects.

In the long run, a "fundamental" theory like the CET requires empirical modification in order to be of general use as a predictive tool. An empirical approach from the outset seems better, thus keeping the functional relations among the parameters as simple as possible.

For concrete and rock, a stress equation of the form

$$\sigma = a + bV \tag{A.2}$$

does seem adequate for correlating penetration data obtained with a given projectile/target combination. In general, however, the coefficients a and b will vary with the characteristics of the projectile and the target. Based on penetration tests in concrete (Reference 18) and intact rock (Reference 19), the following empirical formula is proposed for the stress distribution on the projectile[1]

[1] All dimensional quantities must be expressed in compatible units; e.g., slugs, feet, and seconds.

$$\sigma = 1.582 \left(4Y + 3V\sqrt{\rho Y}\right) \sqrt{\sin \eta} \qquad (A.3)$$

Relating Equation A.3 to A.2, it is clear that $a = 6.328\ Y \sqrt{\sin \eta}$ and that $b = 4.746 \sqrt{\rho Y \sin \eta}$. When Equation A.3 is substituted into Equations 2.4 and 2.8, the equation of motion (Equation 2.10, $\theta = 0$) for a fully embedded projectile becomes

$$M\ddot{Z} = -\frac{\pi D^2}{4\ N_{rc}} \left(4Y + 3V\sqrt{\rho Y}\right) \qquad (A.4)$$

where D is the maximum diameter and N_{rc} is the nose performance coefficient in rock and concrete, given for ogives by

$$N_{rc} = 0.863 \left[\frac{4(CRH)^2}{4CRH - 1}\right]^{1/4} \qquad (A.5)$$

and for cones by

$$N_{rc} = \frac{0.805}{\sqrt{\sin \eta_c}} \qquad (A.6)$$

with η_c representing the cone half-angle and CRH representing the radius of curvature of the tangent ogive in calibers (multiples of D).

Disregarding the changing cross section during the nose-embedment process, the final-depth solution to Equation A.4 is

$$Z_{max} = \frac{4\ N_{rc}\ M}{\pi \rho\ D^2} \left[\frac{V_o}{3} \sqrt{\frac{\rho}{Y}} - \frac{4}{9} \ln \left(1 + \frac{3}{4} V_o \sqrt{\frac{\rho}{Y}}\right)\right] \qquad (A.7)$$

where V_o is the impact velocity.

In addition to the parameters given in Equation A.7, there is at least one more parameter that influences penetrability. In rock this quantity is the Rock Quality Designation (RQD), introduced by Deere (Reference 20). The RQD, an index for the degree of in situ fracturing in a given site, is obtained using a modified core-logging procedure:

> All solid pieces of core that are 4 inches long or longer are added up, and this length is called the modified core recovery. The modified core recovery is divided by the total length of core run, and the quotient multiplied by 100 percent is the value of the RQD.

In concrete, the maximum size of coarse aggregate D_{ag} apparently has a mild effect on penetrability (Reference 21), via the ratio D_{ag}/D .

Letting Y represent the intact unconfined strength for rock and concrete, the effective strengths for penetration can be calculated from

$$Y_r = Y \cdot \left(\frac{RQD}{100}\right)^{0.2} \tag{A.8}$$

$$Y_c = Y \cdot \left(\frac{3D_{ag}}{D}\right)^{0.2} \tag{A.9}$$

Thus, to calculate penetration in less-than-intact rock (RQD < 100), the quantity Y_r should replace Y in Equations A.3, A.4, A.7, and 2.12. Likewise, when the maximum aggregate size is specified for a given concrete, Y_c should replace Y in the same equations.[2]

Figure A.1 shows a comparison of Equation A.7 with nondimensionalized penetration data for rock and concrete. The concrete data were obtained for a case in which $D/D_{ag} = 3$; i.e., $Y_c = Y$. Primarily, the figure shows the degree to which Equation A.7 is able to collapse the data to a single curve. There is some residual scatter, but this correlation represents an improvement over previous attempts (References 4 and 22).[3] Table A.1 presents the data in dimensional form, whereas Table A.2 gives the target properties and projectile parameters.

A.2 EXTRAPOLATION TO NON-NORMAL IMPACT

Equation A.3 was obtained by starting with Equation A.2 and

---

[2] In structural concrete, D_{ag} usually varies from 0.75 to 1.5 inches. The RQD is always assumed to be 100 for concrete.

[3] The improvement comes from the addition of a nose-shape effect and the reduction of the RQD effect initially used in References 4 and 22.

adjusting coefficients until a good data fit was achieved for combined rock and concrete penetration data (Figure A.1) taken from References 18, 19, and 23.[4] Previous experience with these materials had shown that a and b should be proportional to Y and $\sqrt{\rho Y}$, respectively; the $\sqrt{\sin \eta}$-proportionality (nose-shape effect) was drawn from Young's observations of soil penetration and was presumed to hold true for harder targets. With the addition of the RQD effect on the apparent strength, the correlation shown in Figure A.1 was achieved.

The form of Equation A.3 is such that it can readily be extrapolated to the case of nonaxial motion. Recognizing that for axial motion

$$\sin \eta = \frac{V_n}{V} \tag{A.10}$$

where V_n = component of V normal to projectile surface, it is reasonable to replace V and V_n , respectively, by the local velocity v and its normal component v_n .[5] Thus, for 2- or 3-dimensional motion, the expression for the compressive normal stress on the projectile surface is

$$\sigma = 1.582 \left(4Y + 3v\sqrt{\rho Y}\right) \sqrt{\frac{v_n}{v}} \tag{A.11}$$

where

v = absolute local velocity relative to fixed target

v_n = component of v normal to projectile surface

In order for a stress to act on a given projectile surface element, there must be contact with the target (Section 2.4) and net motion into the target ($v_n > 0$). Otherwise, it is presumed that $\sigma = 0$.

---

[4] Additional material property information is given in References 24-26.
[5] For purely axial motion, V and V_n are identical with v and v_n , respectively. In extrapolating to a local definition of stress for nonaxial motion, the most direct route is to use the local velocity.

Table A.1. Penetration data for rock and concrete.

Test Source	Target Material	Impact Velocity fps	Penetration Depth in
Canfield and Clator	Concrete	1005	8.0
Canfield and Clator	Concrete	1025	9.0
Canfield and Clator	Concrete	1250	10.0
Canfield and Clator	Concrete	1485	14.5
Canfield and Clator	Concrete	1775	16.5
Canfield and Clator	Concrete	1975	23.5
Canfield and Clator	Concrete	2020	19.5
Canfield and Clator	Concrete	2325	26.0
Canfield and Clator	Concrete	2350	24.0
Canfield and Clator	Concrete	2430	27.5
Canfield and Clator	Concrete	2535	29.0
Canfield and Clator	Concrete	2655	29.5
Sandia/DNA	Welded Tuff	1220	87
Sandia/DNA	Welded Tuff	1350	102
Sandia/DNA	Welded Tuff	1560	142
Sandia/DNA	Welded Tuff	1640	132
Sandia/DNA	Welded Tuff	1650	132
Sandia/DNA	Sandstone	1455	140
Sandia/DNA	Sandstone	1505	146
Sandia No. 120-77	Welded Agglomerate	1065	156
Sandia No. 120-112	Sandstone	824	122
Sandia No. 120-103	Sandstone	880	120[a]
Sandia No. 120-106	Granite	860	150

[a] In this test the sandstone was covered by 30 inches of soil, so the total depth of penetration is 150 inches. However, the penetration resistance of the soil is negligible compared with that of the rock.

Table A.2. Projectile and target parameters.

Test Source	Projectile Weight lb	Projectile Diameter in	Nose Shape CRH	Target Material	Target Strength psi	Target Density pcf	Target RQD %
Canfield and Clator	13	3.0	1.50	Concrete	5000 ± 5%	142	100
Sandia/DNA	458[a]	6.5	6.00	Welded Tuff	8700 ± 15%	122	100
Sandia/DNA	458[a]	6.5	6.00	Sandstone	3400 ± 30%	130	82
Sandia							
No. 120-77	860	9.0	9.25	Welded Agglomerate	4000 ± 20%	120	60
No. 120-112	2570	10.2	9.25	Sandstone	7100 ± 10%	132	37
No. 120-103	1350	8.0	9.25	Sandstone	5900 ± 5%	134	32
No. 120-106	1350	8.0	9.25	Granite	6700 ± 15%	163	32

[a] The actual projectile weight is 400 lb, but a 116-lb sabot is attached to the projectile base. It is assumed that the projectile and sabot separate about halfway through the penetration process. This makes the "average" projectile weight about 458 lb.

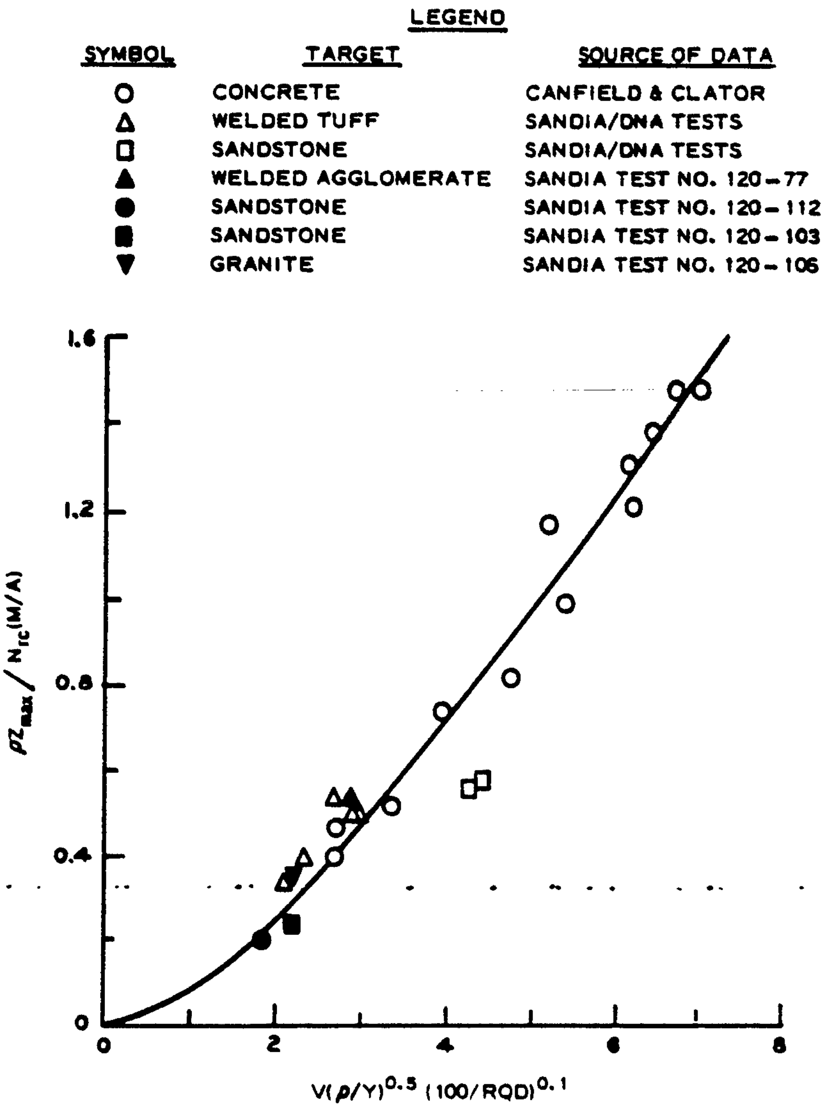

Figure A.1 Nondimensionalized penetration data for rock and concrete.

APPENDIX B

PENETRATION THEORY FOR SOIL

B.1 EMPIRICAL THEORY FOR NORMAL IMPACT

To date, Young's equation (References 1-3) has been the most consistently successful formula for calculating penetration depths in soil. Rather than using standard engineering properties to describe the target, Young lumps the penetrability into a single empirical variable, represented by S . In U. S. customary units,[1] Young's equation is

$$Z_{max} = \begin{cases} 0.0031\ S\ N_s \sqrt{W/A}\left(V_o - 100\right), & V_o \geq 200 \text{ ft/s} \\ 0.53\ S\ N_s \sqrt{W/A}\ \ln\left(1 + \dfrac{2V_o^2}{100{,}000}\right), & V_o < 200 \text{ ft/s} \end{cases}$$

where

Z_{max} = final depth, ft

W = projectile weight, lb

$A = \frac{\pi}{4} D^2$ = maximum cross-sectional area, sq in

V_o = impact velocity, ft/s

N_s = nose performance coefficient in soil, dimensionless

S = soil penetrability index, dimensionless

The S-number can be obtained directly from previous penetration data for a given target, or it can be estimated from data for geologically similar targets (Table B.1). Whatever the case, Young's equation represents a scaling relation between the projectile characteristics (size, weight, geometry), the impact velocity, and the maximum depth of penetration.

Since Young's equation gives only the final depth, it cannot be used to calculate the instantaneous resisting force, only the average resisting force. This is not a drawback for normal impact, since the

---

[1] Young's equation is not dimensionally homogeneous. All quantities must be specified in the units given.

axial resisting force is often a step-pulse (i.e., uniform, except for some oscillation) in a given layer. On the other hand, for non-normal impact, both the axial and lateral forces must be known if the 2- and 3-D motion is to be calculated. Since Young's equation gives no indication of the lateral forces, a more detailed analysis is needed.

In Reference 4 a projectile equation of motion was developed for normal impact and penetration in soil, based on data originally used by Young. Postulating that the axial force should (a) have the form of a step-pulse and (b) exhibit linear dependence on velocity, it was found that an equation of the form

$$-M \frac{dV}{dt} = a + bV + cZ \qquad \text{(B.1)}$$

would satisfy both these criteria, provided that

$$b \propto \sqrt{Mc} \qquad \text{(B.2)}$$

The explicit appearance of the projectile mass in the velocity coefficient b was puzzling but absolutely necessary to generate a step-pulse resisting force. Moreover, it brought the mass dependence of the maximum depth into agreement with Young. Physically, however, the mass should occur only on the left side of Equation B.1, with parameters such as diameter, nose shape, and S-number appearing in the coefficients a, b, and c.

The mass dependence of the coefficient b is now thought to be a size effect in disguise. This is reasonable since many of the larger projectiles used by Young had masses <u>roughly</u> proportional to D^3.[2] Consequently, an alternative to Equation B.2 is

---

[2] The deep earth penetrators, built and tested by Sandia Laboratories, had L/D ratios of about 10 to maintain stability. For many of these projectiles the weight (in pounds) can be related to the maximum diameter (in inches) by

$$W = 1.3\, D^3 \pm 30\%$$

$$b \propto \sqrt{D^3 c} \tag{B.3}$$

In either case, the approximate solution for the final depth Z_{max} is

$$Z_{max} = \frac{1}{c}\left[-\left(a + \frac{2}{3} bV_o\right) + \sqrt{\left(a + \frac{2}{3} bV_o\right)^2 + McV_o^{\,2}}\right] \tag{B.4}$$

and the dependence of a and c upon S and D is the same as in Reference 4:

$$a \propto \frac{D}{S} \tag{B.5}$$

$$c \propto \frac{D^2}{S^2} \tag{B.6}$$

which insures that for low-velocity, shallow penetration,

$$Z_{max} \propto \frac{S}{D} \tag{B.7}$$

in accordance with Young's equation. When the nose performance coefficient N_s is added, the coefficients a , b , and c can be expressed in terms of three "universal" constants μ , β , γ :

$$a = \frac{\mu D}{S N_s} \tag{B.8}$$

$$b = \frac{\sqrt{\beta D^5}}{S N_s} \tag{B.9}$$

$$c = \frac{\gamma D^2}{S^2 N_s^{\,2}} \tag{B.10}$$

With these expressions for a , b , and c , it follows from Equation B.4 that

$$Z_{max} = \frac{S\ N_s}{D^n} \qquad (B.11)$$

where

$$1 \leq n < 2.5 \qquad (B.12)$$

and Young's nose performance coefficient in soil is approximated by

$$N_s \approx 0.632 \left[\frac{4(CRH)^2}{4\ CRH - 1}\right]^{1/4} \text{, ogives} \qquad (B.13)$$

$$N_s \approx \frac{0.548}{\sqrt{\sin \eta_c}} \text{, cones} \qquad (B.14)$$

The values of the constants μ , β , and γ have been obtained. The ratio of β/γ was adjusted until step-pulse deceleration curves were achieved. The values of μ and γ were then determined by fitting Equation B.4 to shallow penetration data (Reference 27) for projectiles with the same weight and diameter[3] in the Main Lake area of Tonopah Test Range (TTR). The values for the three constants[4] are

$$\mu = 1.96 \times 10^5 \text{ lb/ft}$$

$$\beta = 6.25 \times 10^6 \text{ lb}^2\text{s}^2/\text{ft}^7$$

$$\gamma = 1.56 \times 10^5 \text{ lb/ft}^3$$

Figure B.1 compares Equation B.4 with normalized[5] deep- and

---

[3] W = 224 pounds, D = 4.4 inches .

[4] Equations B.1, B.4, B.8–B.10, B.15, and B.16 are dimensionally homogeneous. Any set of dimensionally compatible units may be used therein, as long as all quantities are converted to the same system of units.

[5] Normalized using Equation B.4. Amount of scatter in normalized data indicates degree of validity as scaling relation.

shallow-penetration data for TTR Main Lake. The same data are given in original form in Reference 2, where Young gives the S-number profile as $S = 5.2$ from 0 to 8 feet and $S = 2.5$ from 8 to 25 feet. Equation B.4 agrees best with the shallow data using $S = 4.3$ and with the deep data using $S = 3$.

Equation B.4 appears to do about as well as Young's equation in extrapolating and interpolating soil penetration data, but as a formula for depth prediction, it offers no advantage over the latter. On the other hand, the underlying equation of motion (Equation B.1) contains some additional information concerning the explicit relation between the axial resisting force and the velocity, depth, diameter, and geometry of the projectile.

The analysis of nonaxial motion requires that the stress distribution be specified on the projectile. In the present context, any stress distribution is potentially correct if it generates Equation B.4 with the values of a , b , and c given by Equations B.8-B.10. The simplest distribution that accomplishes this, giving approximately the right dependence of N_s on projectile geometry, is a compressive normal stress defined as follows:

$$\sigma = \frac{0.625\ \mu}{S\ r_p}\sqrt{\sin\eta} + \frac{5.19\ V}{S}\sqrt{\beta\ r_p\ \sin\eta} + \frac{5.9\ \gamma Z}{S^2}\sin\eta \qquad (B.15)$$

where

r_p = local cylindrical radius of projectile

η = local angle between projectile surface and axis of symmetry (Figure 2.1)

Z = vertical depth from target surface to point on projectile surface (Figure 2.7)

B.2 EXTRAPOLATION TO NON-NORMAL IMPACT

Now that the stress distribution is defined by Equation B.15, the extrapolation procedure for soil is the same as for rock and concrete (Appendix A). Thus, for 2- or 3-D motion, the function $\sin\eta$ is replaced by v_n/v , and V by v , so that

$$\sigma = \frac{0.625\ \mu}{S\ r_p}\sqrt{\frac{v_n}{v}} + \frac{5.19\ v}{S}\sqrt{\beta\ r_p\ \frac{v_n}{v}} + \frac{5.9\ \gamma Z}{S^2}\ \frac{v_n}{v} \tag{B.16}$$

As in Appendix A, it is assumed that for a stress to act on a given projectile surface element there must be contact with the target (Section 2.4) and net motion into the target ($v_n > 0$), otherwise $\sigma = 0$.

Table B.1. Typical S-numbers for natural earth materials.[a]

S	Materials
1-2	Frozen silt or clay, saturated, very hard. Rock, weathered, low strength, fractured. Sea or freshwater ice more than 10 feet thick.
2-3	Massive gypsite deposits.[b] Well-cemented coarse sand and gravel. Caliche, dry. Frozen, moist silt or clay.
4-6	Sea or freshwater ice from 1 to 3 feet thick. Medium dense, medium to coarse sand, no cementation, wet or dry. Hard, dry, dense silt or clay.[c] Desert alluvium.
8-12	Very loose, fine sand, excluding topsoil. Moist, stiff clay or silt, medium dense, less than about 50 percent sand.
10-15	Moist topsoil, loose, with some clay or silt. Moist, medium stiff clay, medium dense, with some sand.
20-30	Loose, moist topsoil with humus material, mostly sand and silt. Moist to wet clay, soft, low shear strength.
40-50	Very loose, dry, sandy topsoil (Eglin AFB). Saturated, very soft clay and silts, with very low shear strengths and high plasticity.[d] Wet lateritic clays.

[a] Taken from Reference 3.
[b] White Sands Missile Range, New Mexico.
[c] Tonopah Test Range, Nevada, dry lake playas.
[d] Great Salt Lake Desert and bay mud at Skaggs Island.

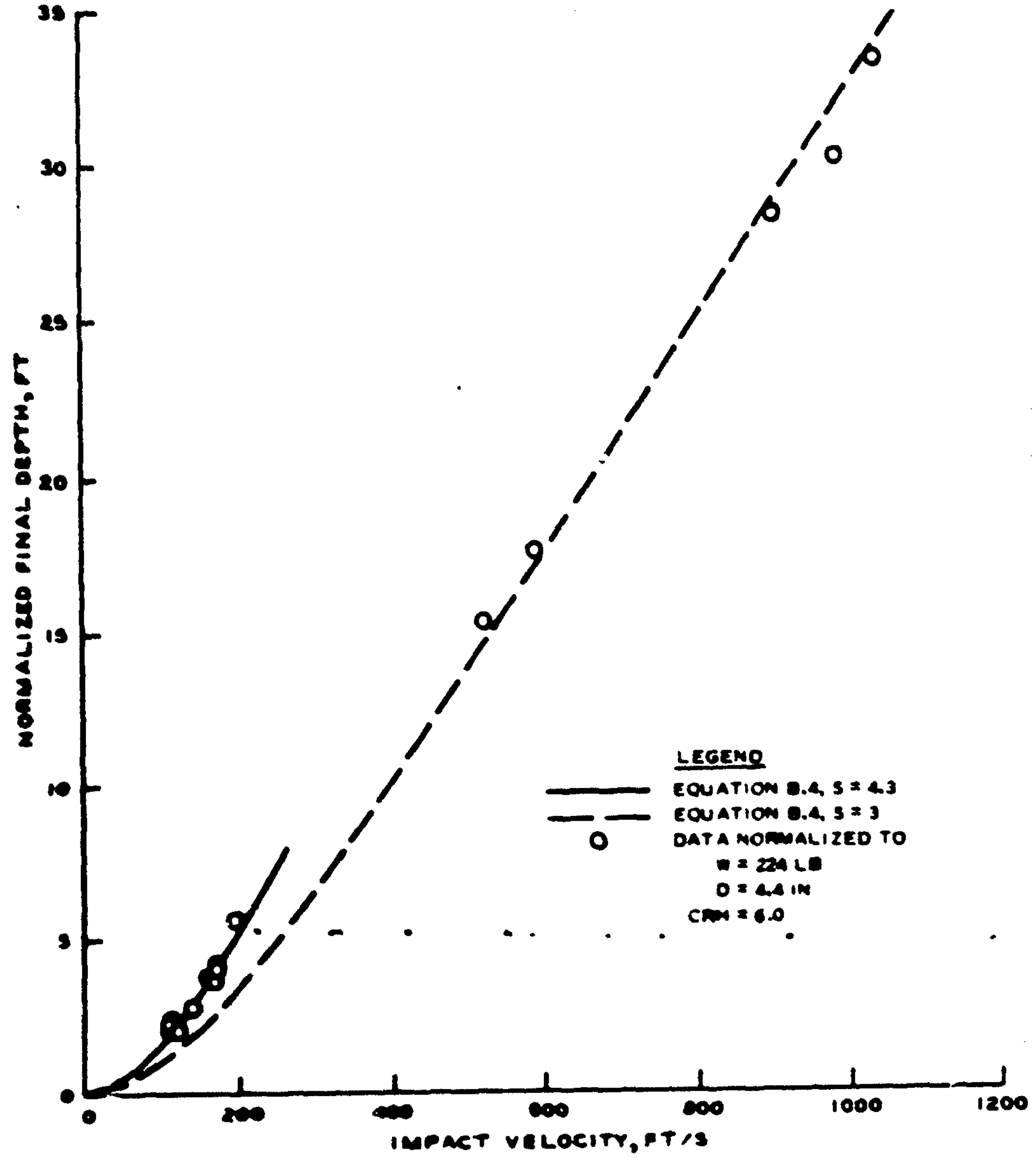

Figure B.1 Comparison of calculated penetration depths with data from TTR Main Lake area.

APPENDIX C

NOTATION

a, b, c	Empirical force coefficients
A	Maximum cross-sectional area of projectile
CRH	Tangent-ogive radius of curvature, in calibers ("caliber radius head")
dA	Differential element of surface area on projectile
dF_x, dF_z	Differential force components in the body-fixed lateral and axial (x- and z-) directions, respectively
D	Maximum projectile diameter
D_{ag}	Maximum coarse aggregate size
f(V)	Function of velocity
F_x, F_z	Net force components in the body-fixed lateral and axial (x- and z-) directions, respectively
g	Gravitational acceleration (32.2 ft/s^2)
I	Transverse mass moment of inertia about CG
k	Free-surface parameter, r_s/r_p
L	Projectile length
M	Projectile mass, W/g
n	Exponent
N_{rc}	Nose performance coefficient in rock and concrete
N_3	Nose performance coefficient in soil
r_c	Cylindrical radius of wake cavity
r_o	Cylindrical radius of projectile at separation point
r_p	Local cylindrical radius on projectile surface at a given point
r_s	Maximum perpendicular distance from projectile axis, through dA , to target surface, for which stress relief can occur due to free-surface effect

RQD	Rock quality designation
S	Soil penetrability index
t	Time[1]
v	Absolute local velocity of any point on projectile surface
v_n	Outward normal component of local velocity
v_x, v_z	Local velocity components in body-fixed lateral and axial (x- and z-) directions, respectively
V	Projectile CG velocity
V_n	Outward normal component of CG velocity
V_o	Impact velocity
V_x, V_z	Components of CG velocitv in body-fixed lateral and axial (x- and z-) directions, respectively
W	Projectile weight
x	Lateral (body-fixed) position in projectile
X	Horizontal position in target
$\ddot{X}$, $\ddot{Z}$	Components of acceleration in the X- and Z-directions, respectively
Y	Unconfined compressive strength of intact rock or concrete
Y_c	Concrete strength, corrected for aggregate size
Y_r	Rock strength, corrected for RQD
z	Axial (body-fixed) position in projectile, measured forward from CG
Z	Vertical position (depth) in target, measured downward from target surface
Z_{CG}	Vertical position (depth) of CG, measured downward from target surface
Z_{max}	Maximum (final) depth of penetration of nose tip

[1] A dot over any quantity indicates differentiation with respect to time.

α	Angle of attack
α_o	Initial angle of attack
β	Constant, 6.25×10^6 lb^2-s^2/ft^7
γ	Constant, 1.56×10^5 lb/ft^3
δ	Lateral displacement of point on projectile axis, relative to wake cavity
δ_o	Initial displacement of point on projectile axis
ζ	Axial distance aft of the nose tip
ζ_o	Axial distance from nose tip to separation point
ζ_{CG}	Axial distance from nose tip to CG
η	Local angle between projectile axis and line tangent to projectile surface
η_c	Cone half-angle
θ	Obliquity angle, measured counterclockwise from target-fixed Z-axis to projectile-fixed z-axis
$\dot{\theta}$	Angular velocity
$\ddot{\theta}$	Angular acceleration
θ_o	Initial obliquity angle
μ	Constant, 1.96×10^5 lb/ft
ρ	Mass density of rock or concrete
σ	Local compressive normal stress on projectile surface
σ_x, σ_z	Components of local compressive normal stress in body-fixed lateral and axial (x- and z-) directions, respectively
ϕ	Local angle of approach between projectile surface element and target, based on CG velocity components
ϕ_{aft}	Aftbody flare angle
ϕ_{min}	Angle of approach at which separation occurs (wake separation angle)
ψ	Azimuthal angle on projectile

DISTRIBUTION LIST

DEPARTMENT OF DEFENSE

Assistant to the Secretary of Defense,
Atomic Energy,
ATTN: Donald R. Cotter

Director, Defense Advanced Research
Projects Agency,
ATTN: COL B. Pafe
NMRO
Paul C. McMonigal
CDR J. Beatty
LTC M. Franklin
S. Lukasik
PMO
STO
Eric H. Willis
Technical Library

Federal Emergency Management Agency
ATTN: Director

Defense Documentation Center, Cameron Station
12 cy ATTN: TC/Myer B. Kahn

Director, Defense Intelligence Agency
ATTN: DI-7E
DT-2, Weapons & Systems Division
DI-7D, Phys. Vul. Div.,
Edward O'Farrell
Technical Library

Defense Mapping Agency
ATTN: H. Lindsey

Director, Defense Nuclear Agency
ATTN: STSI (Archives)
2 cy STTL (Technical Library)
15 cy SPSS
DDST

Director of Defense Research and Engineering
ATTN: Assistant Director, Strategic
Weapons
Deputy Director, Strategic
Systems
M. J. Minneman
George Barse
Craig W. Hartsell
R. Thorkildsen
Deputy Director, Tactical Warfare

Commander, Field Command, Defense Nuclear
Agency
ATTN: FCPR

Interservice Nuclear Weapons School
ATTN: Technical Library

Director, Joint Strategic Target Planning
Staff, JCS
ATTN: Science and Technology Info
Library

Director, Weapons Systems Evaluation Group
ATTN: Technical Library

DEPARTMENT OF THE ARMY

Director, U. S. Army Ballistic Missile
Defense Advanced Technology Center
ATTN: BMDATC-X
CRDABH-S

Ballistic Missile Defense Program Manager, U. S.
Army Ballistic Missile Defense Program Office
ATTN: DACS-BMT/Dr. John Shea

Headquarters, Central Army Group
ATTN: CENEN LTC J. L. Spruill

Office, Chief of Engineers
2 cy ATTN: DAEN-ASI-L
2 cy DAEN-MCE-D
DAEN-RDL

Office, Chief of Research, Development, and
Acquisition
ATTN: DAMA-CSM
Technical Library

Commander, Harry Diamond Laboratories
ATTN: A. Holmes
AMXDO-NP
AMXDO-RBH/J. Gwaltney

Project Manager, Remotely Monitored Battlefield
Sensor System, U. S. Army Materiel Development
and Readiness Command (DARCOM)
ATTN: Chuck Higgins

Commanding Officer, Picatinny Arsenal
ATTN: Paul Harris
P. Angelloti
Technical Library
SMUPA-ND-S/E. Zimpo
William Meyer
Ray Goldstein
Ray Moessner
Marty Margolin
Jerry Pental
SUMPA-AD-D-A-7
SUMPA-AD-D-A
SUMPA-AD-D-M

Director, U. S. Army Ballistic Research
Laboratories
ATTN: AMXBR-X/J. J. Meszaros
J. H. Keefer
AMXBR-TB/J. T. Frasier
W. J. Taylor
Norris J. Huffington, Jr.
D. Dunn
G. Grabarek
B. Reiter
G. Roecker
2 cy Technical Library/Edward Baicy
J. W. Apgar
R. Paul Ryan, Chief, Closed
Literature, Scientific and Tech-
nical Information Branch

Commander/Director, U. S. Army Cold Regions
Research and Engineering Laboratory
ATTN: G. Swinzow

DEPARTMENT OF THE ARMY (Continued)

Division Engineer, U. S. Army Engineer Division,
Huntsville
ATTN: HNDED-CS/Michael M. Dembo

District Engineer
U. S. Army Engineer District, St. Paul
ATTN: Library

Division Engineer, U. S. Army Engineer Division,
Ohio River
ATTN: ORDAS-L/Technical Library

Director, U. S. Army Engineer Waterways
Experiment Station
ATTN: Mr. L. F. Ingram
Mr. L. K. Davis
Mr. William J. Flathau
Mr. John Strange
3 cy Library
Dr. Paul Hadala
Dr. Guy Jackson
Dr. Behzad Rohani
Mr. Allen D. Rooke

Commander, U. S. Army Materials and Mechanics
Research Center
ATTN: John Mescall
Technical Library
Richard Shea

Director, U. S. Army Material Systems Analysis
Agency
ATTN: J. Sperazza
M. Reches

Commander, U. S. Army Mobility Equipment
R&D Center
ATTN: STSFB-MW
STSFB-XS
Technical Library

Commandant, U. S. Army Engineer School
ATTN: ATSEN-SY-L

Commander, U. S. Army Materiel Development
and Readiness Command, (DARCOM)
Research and Concepts Branch

Commander, U. S. Army Nuclear Agency
ATTN: Document Control
Technical Library
COL Quinn
MAJ F. P. Weichel

Commander, U. S. Army Missile Command
ATTN: Technical Library
F. Fleming
AMCPM-PE-X (William K. Jann)

Commander, U. S. Army Armament Command
ATTN: Technical Library

Division Engineer, U. S. Army Engineer
Division, Missouri River
ATTN: Library

DEPARTMENT OF THE NAVY

Chief of Naval Research, Department of
the Navy
ATTN: Technical Library

Officer in Charge, Civil Engineering Laboratory,
Naval Construction Battalion Center
ATTN: R. J. Odello
Technical Library

Commander, Naval Electronics Systems Command,
Headquarters
ATTN: PME-117-21A

Commander, Naval Facilities Engineering Command
ATTN: Technical Library, Code 0911C

Superintendent, U. S. Naval Postgraduate School
ATTN: Library, Code 2124

Director, Naval Research Laboratory
ATTN: Code 2027/Tech Library

Commander, Naval Surface Weapons Center
ATTN: Mr. Kasdorf
Technical Library
Code 1224 Navy Nuc Prgms Off
Jules Enig
Mary P. King
L. Roslund
Robert D. Heidenreich
G. Briggs
Technical Library
William Wisherd
Ted Williams
M. Weiland

Commander, Naval Weapons Center
ATTN: Code 603, Dr. Carl Austin
Mr. P. Cordle
Code 533, Technical Library

Commander, Naval Weapons Evaluation Facility
ATTN: Technical Library

Director, Strategic Systems Project Office,
Navy Department
2 cy ATTN: NSP-43, Technical Library

DEPARTMENT OF THE AIR FORCE

Air Force Armament and Testing Laboratory, AFSC
ATTN: Technical Library
MAJ Thomas Tomasetti
3 cy Mr. John Collins
Mr. Leonard Wilson
Mr. Masey Valentine
Mr. William Cramer
Dr. Kulp

Air Force Institute of Technology
ATTN: Technical Library

Commander, Air Force Weapons Laboratory, AFSC
ATTN: SUL, Technical Library
DEV-S/Dr. M. A. Plamondon

DEPARTMENT OF THE AIR FORCE (Continued)

Headquarters, Air Force Systems Command
ATTN: Technical Library

Project Manager, Gator Mine Program
ATTN: E. J. Lindsey

Oklahoma State University, Field Office for Weapons Effectiveness
ATTN: Ed Jackett

Air Force Office of Scientific Research
ATTN: LTC L. P. Mosteller, Jr.

Commander, Rome Air Development Center, AFSC
ATTN: EMTLD, Documents Library

Commander, Armament Development and Test Center
ATTN: ADTC/DLODL/Technical Library

Commander, Foreign Technology Division, AFSC
ATTN: TD-BTA Library

HQ USAF/IN
ATTN: INATA

HQ USAF/RD
ATTN: RDPM, COL J. E. McCormick

Space and Missile Systems Organization
ATTN: DEB

ENERGY RESEARCH & DEVELOPMENT ADMINISTRATION

U. S. Energy Research and Development Administration, Division of Military Application
ATTN: Doc Control for Test Office

U. S. Energy Research and Development Administration, Albuquerque Operations Office
ATTN: Doc Control for Technical Library

U. S. Energy Research and Development Administration, Division of Headquarters Services, Library Branch G-043
ATTN: Doc Control for Class Tech Lib

U. S. Energy Research and Development Administration, Nevada Operations Office
ATTN: Doc Control for Technical Library

Los Alamos Scientific Laboratory
ATTN: Doc Control for Reports Library
Doc Control for Tom Dowler
Doc Control for C. Cremer
Doc Control for G. Dials

Sandia Laboratories
ATTN: Doc Control for T. Gold
Doc Control for Technical Library
Doc Control for Dr. Walter Herrman
Doc Control for John Colp
Doc Control for John Keizur, Org. No. 1312
Doc Control for William Patterson
Doc Control for Al Chabai
Doc Control for 3141 Sandia Rpt Coll
Doc Control for Ray Reynolds

ENERGY RESEARCH & DEVELOPMENT ADMINISTRATION (Continued)

Director, Lawrence Livermore Laboratory
ATTN: Technical Information Division, Technical Library
Larry Woodruff, L-125
Doc Control for W. Scanlin
Frank Walker
Mark Wilkins

OTHER GOVERNMENT AGENCIES

Electric Power Research Institute
ATTN: Dr. George Sliter

Office of Nuclear Reactor Regulation, Nuclear Regulatory Commission, Division of Technical Review
ATTN: Mr. Lawrence Shao, Chief, Struc Engrg Br

Bureau of Mines, Twin Cities Research Center
ATTN: R. E. Thill

DEPARTMENT OF DEFENSE CONTRACTORS

Aerospace Corporation
ATTN: Technical Information Services
R. Strickler
George Young

Agbabian Associates
ATTN: Dr. M. S. Agbabian

Applied Theory Incorporated
2 cy ATTN: Dr. John G. Trulio

AVCO, Government Products Group
ATTN: David Henderson
Frank Lasher
Research Library A830, Room 7201
John Atanasoff

Battelle Columbus Laboratories
ATTN: Technical Library

Bell Telephone Laboratories, Inc.
ATTN: Technical Report Center

Boeing Company
ATTN: Aerospace Library
Reynold Atlas

California Research and Technology, Inc.
ATTN: Dr. K. N. Kreyenhagen
Technical Library

Civil/Nuclear Systems Corporation
ATTN: Robert Crawford

EG&G, Inc.
ATTN: Technical Library

General Dynamics Corporation
ATTN: Keith Anderson

General Electric Company, TEMPO-Center for Advanced Studies
ATTN: DASIAC

DEPARTMENT OF DEFENSE CONTRACTORS (Continued)

IIT Research Institute
ATTN: Technical Library

Institute for Defense Analyses
ATTN: IDA Librarian Ruth S. Smith

Consulting and Special Engineering Services, Inc.
ATTN: Dr. J. L. Merritt
Technical Library

Kaman Avidyne, Division of Kaman Sciences Corp.
ATTN: Technical Library
E. S. Crisicone
N. P. Hobbs

Kaman Sciences Corporation
ATTN: Technical Library

Lockheed Missiles and Space Company
ATTN: Tech Info Center D/Coll
Technical Library

Martin Marietta Aerospace
ATTN: M. Anthony
Gerbert E. McQuaig (MP-81)

University of Illinois
ATTN: Dr. Nathan M. Newmark

University of New Mexico
ATTN: H. D. Southward
G. E. Triandafalidis

Physics International Company
ATTN: Doc Control for Mr. Fred M. Sauer
Doc Control for Dr. Robert Swift
Doc Control for Technical Library
Doc Control for Mr. Dennis L. Orphal
Doc Control for Mr. Larry Behrman

R&D Associates
ATTN: Dr. Harold L. Brode
Dr. H. F. Cooper, Jr.
Mr. R. J. Port
Technical Library
Mr. William B. Wright
Dr. C. P. Knowles
Mr. J. G. Lewis

Science Applications, Inc.
ATTN: Mr. David Bernstein
Dr. D. E. Maxwell
Dr. Cecil Ivan Hudson, Jr.
Dr. W. M. Layson

Stanford Research Institute
ATTN: Dr. Carl Peterson
Dr. G. Abrahamson
Mr. Lynn Seamans
SRI Library Room G021

DEPARTMENT OF DEFENSE CONTRACTORS (Continued)

Systems, Science and Software
ATTN: Dr. Donald R. Grine
Technical Library

Terra Tek, Inc., University Research Park
ATTN: Mr. S. J. Green
Dr. A. H. Jones
Technical Library

Texas A&M University
ATTN: Harry Coyle
Prof. L. J. Thompson

TRW Defense and Space Systems Group
ATTN: Tech Info Center/S-1930

Weidlinger Associates, Consulting Engineers
ATTN: Dr. Melvin L. Baron
Mr. J. W. Wright
Dr. J. Isenberg

Lowell Technical Institute, Department of Civil Engineering
ATTN: L. W. Thigpen

Georgia Institute of Technology, Department of Aerospace Engineering
ATTN: S. V. Hanagud
L. N. Rehfield

Engineering Societies Library
ATTN: Acquisitions Librarian

Pacific Technology, Inc.
ATTN: G. I. Kent
R. L. Bjork

FOREIGN EXCHANGES

Regierungsrat, Bundesanstalt fur Strassenwesen

Department of Physical Geography, Uppsala University

Prof. Leopold Muller, Abteilung Felsmechanik, Institut fur Bodenmechanik und Felsmechanik, Universitat Karlsruhe

DOMESTIC EXCHANGE

Tennessee Valley Authority
ATTN: Ronald G. Domer, Chief, Civil Engineering Branch

In accordance with letter from DAEN-RDC, DAEN-ASI dated 22 July 1977, Subject: Facsimile Catalog Cards for Laboratory Technical Publications, a facsimile catalog card in Library of Congress MARC format is reproduced below.

Bernard, Robert S
Projectile penetration in soil and rock: analysis for non-normal impact / by Robert S. Bernard, Daniel C. Creighton. Vicksburg, Miss. : U. S. Waterways Experiment Station ; Springfield, Va. : available from National Technical Information Service, 1979.
88 p. : ill. ; 27 cm. (Technical report - U. S. Army Engineer Waterways Experiment Station ; SL-79-15)
Prepared for Defense Nuclear Agency, Washington, D. C., under DNA Subtask Y99QAXSB211, Work Unit 20.
References: p. 61-63.

1. Ballistics. 2. Computer analysis. 3. Impact. 4. Numerical analysis. 5. Penetration. 6. Projectiles. 7. Rock penetration. 8. Soil penetration. I. Creighton, Daniel C., joint author. II. United States. Defense Nuclear Agency. III. Series: United States. Waterways Experiment Station, Vicksburg, Miss. Technical report ; SL-79-15.
TA7.W34 no.SL-79-15